

Exploring Cosmic Dawn with PANORAMIC II: Cosmic Variance and Galaxy Clustering at $z \sim 10$

ANDREA WEIBEL,^{1,*} CHRISTIAN KRAGH JESPERSEN,^{2,*} PASCAL A. OESCH,^{1,3,4} CHRISTINA C. WILLIAMS,^{5,6}
 RACHEL BEZANSON,⁷ GABRIEL BRAMMER,^{3,4} AIDAN P. CLOONAN,⁸ PRATIKA DAYAL,^{9,10,11} ANNE HUTTER,¹² ZHIYUAN JI,⁶
 MICHAEL V. MASEDA,¹³ MARKO SHUNTOV,^{3,4,1} AND KATHERINE E. WHITAKER^{8,3}

¹Department of Astronomy, University of Geneva, Chemin Pegasi 51, 1290 Versoix, Switzerland

²Department of Astrophysical Sciences, Princeton University, Princeton, NJ 08544, USA

³Cosmic Dawn Center (DAWN), Denmark

⁴Niels Bohr Institute, University of Copenhagen, Jagtvej 128, København N, DK-2200, Denmark

⁵NSF National Optical-Infrared Astronomy Research Laboratory, 950 North Cherry Avenue, Tucson, AZ 85719, USA

⁶Steward Observatory, University of Arizona, 933 North Cherry Avenue, Tucson, AZ 85721, USA

⁷Department of Physics and Astronomy and PITT PACC, University of Pittsburgh, Pittsburgh, PA 15260, USA

⁸Department of Astronomy, University of Massachusetts, Amherst, MA 01003, USA

⁹Canadian Institute for Theoretical Astrophysics, 60 St George St, University of Toronto, Toronto, ON M5S 3H8, Canada

¹⁰David A. Dunlap Department of Astronomy and Astrophysics, University of Toronto, 50 St George St, Toronto ON M5S 3H4, Canada

¹¹Department of Physics, 60 St George St, University of Toronto, Toronto, ON M5S 3H8, Canada

¹²Institute for Astronomy, University of Vienna, Türkenschanzstrasse 17, A-1180 Vienna, Austria

¹³Department of Astronomy, University of Wisconsin-Madison, 475 N. Charter St., Madison, WI 53706 USA

ABSTRACT

Observational campaigns with JWST have revealed a higher-than-expected abundance of UV-bright galaxies at $z \gtrsim 10$, with various proposed theoretical explanations. A powerful complementary constraint to break degeneracies between different models is galaxy clustering. In this paper, we combine PANORAMIC pure parallel and legacy imaging along 34 independent sightlines to measure the cosmic variance (σ_{CV}) in the number counts of Lyman break galaxies at $z \sim 10$ which is directly related to their clustering strength. We find $\sigma_{\text{CV}} = 0.96_{-0.18}^{+0.20}$, $1.46_{-0.44}^{+0.54}$, and $1.71_{-0.59}^{+0.72}$ per NIRCam pointing ($\sim 9.7 \text{ arcmin}^2$, $\lesssim 1.5 \text{ pMpc}$ at $z \sim 10$) for galaxies with $M_{\text{UV}} < -19.5$, -20 , and -20.5 . Comparing to galaxies in the fiducial **UniverseMachine**, we find that σ_{CV} is consistent with our measurements, but that the number densities are a factor $\gtrsim 5$ lower. We implement simple models in the **UniverseMachine** that represent different physical mechanisms to enhance the number density of UV-bright galaxies. All models decrease σ_{CV} by placing galaxies at fixed M_{UV} in lower mass halos, but to varying degrees. Combined constraints on σ_{CV} and the UVLF thus tentatively disfavor models that globally increase the star formation efficiency (SFE) or the scatter in the $M_{\text{UV}}-M_{\text{halo}}$ relation, while models that decrease the mass-to-light ratio, or assume a power-law scaling of the SFE with M_{halo} agree better with the data. We show that with sufficient additional independent sightlines, robust discrimination between models is possible, paving the way for powerful constraints on the physics of early galaxy evolution through NIRCam pure parallel imaging.

Keywords: Galaxy photometry (611), High-redshift galaxies (734), Cosmic web (330), Clustering (1908), Galaxy evolution (594), James Webb Space Telescope (2291)

1. INTRODUCTION

Corresponding author: Andrea Weibel (andrea.weibel@unige.ch) & Christian Kragh Jespersen (ckragh@princeton.edu)

* These authors contributed equally to this work.

One of the biggest surprises that the James Webb Space Telescope (JWST) has brought us over the last few years is the high number of luminous $z \gtrsim 10$ galaxies that it revealed through deep imaging (e.g. Naidu et al. 2022; Castellano et al. 2022; Adams et al. 2023; Finkelstein et al. 2023; Atek et al. 2023; Casey et al. 2024; Hainline et al. 2024), and confirmed spectroscopically

(e.g. Arrabal Haro et al. 2023; Curtis-Lake et al. 2023; Castellano et al. 2024; Fujimoto et al. 2024; Harikane et al. 2024; Carniani et al. 2024; Naidu et al. 2025). Statistical measurements of the UV luminosity function (UVLF) at $z \gtrsim 10$ from various imaging programs and fields (e.g. Donnan et al. 2023; Pérez-González et al. 2023; Harikane et al. 2023; Adams et al. 2024; Finkelstein et al. 2024; Robertson et al. 2024; Donnan et al. 2024; Whitler et al. 2025; Weibel et al. 2025) therefore yielded an excess at the bright end, and a shallow evolution with redshift compared to (extrapolations of) pre-JWST measurements (e.g. Bouwens et al. 2016; Ishigaki et al. 2018; Oesch et al. 2018), and theoretical expectations (e.g. Dayal et al. 2014; Mason et al. 2015; Tacchella et al. 2018; Williams et al. 2018; Behroozi et al. 2019; Steinhardt et al. 2021).

A wealth of models that can explain this high abundance of UV-bright galaxies have been discussed in the literature. This includes models that boost the observed UV-luminosity of galaxies at fixed halo mass through e.g. a more top-heavy initial mass function (IMF; Yung et al. 2024; Trinca et al. 2024; Cueto et al. 2024; Lu et al. 2025; Mauerhofer et al. 2025; Hutter et al. 2025), a higher star formation efficiency (SFE; Dekel et al. 2023; Li et al. 2024; Boylan-Kolchin 2024; Mauerhofer et al. 2025; Somerville et al. 2025), a lack of dust attenuation (Ferrara et al. 2023), or an AGN-contribution to the UV-luminosity (Pacucci et al. 2022; Hegde et al. 2024). Using the FIREBox^{HR} simulation, Feldmann et al. (2025) showed that the UVLF and the UV luminosity density at $z \sim 6 - 14$ can also be reproduced based on just a weakly halo mass dependent SFE. A different class of models increases the scatter in the $M_{\text{UV}}-M_{\text{halo}}$ relation, in particular through enhanced burstiness in the star formation histories (SFHs) of high redshift galaxies (Mason et al. 2023; Shen et al. 2023; Sun et al. 2023; Kravtsov & Belokurov 2024). Crucially, while these models all boost the number density of galaxies, they have different implications for their clustering strength. Hence they can in principle be distinguished based on clustering measurements (e.g. Muñoz et al. 2023; Gelli et al. 2024; Shuntov et al. 2025).

Observational results regarding the abundance of UV-bright galaxies at $z \gtrsim 10$ are usually based on a small number of independent lines of sight. They are therefore subject to significant cosmic variance, which describes fluctuations in the number density of galaxies because of their clustering in the cosmic web (e.g. Moster et al. 2011; Jespersen et al. 2025c). Indeed, determinations of the UVLF based on a larger number of independent sightlines, and/or using data outside of the commonly studied legacy fields found somewhat lower number den-

sities at $z \gtrsim 10$ (e.g. Willott et al. 2024; Morishita et al. 2025; Asada et al. 2025). Nevertheless, the impact of cosmic variance on JWST-based results remains large due to its limited field of view, and the fact that many studies build on a small number of legacy fields containing most of the data.

Weibel et al. (2025, W25 hereafter) recently combined legacy imaging with pure parallel imaging from PANORAMIC (GO-2514, PIs Williams & Oesch, Williams et al. 2025) to measure UVLFs at $z \sim 10$, $z \sim 13$, and $z \sim 17$ along 35 independent lines of sight. This work confirmed the high abundance of UV-bright ($M_{\text{UV}} \lesssim -21$) galaxies at $z \sim 10$ and $z \sim 13$, but found a more rapid evolution in the UVLF than previous studies, corresponding to a drop in the UV luminosity density by a factor $> 50 \times$ from $z \sim 10$ to $z \sim 17$. Many recently proposed theoretical models are consistent with these findings but cannot be distinguished solely based on the UVLF.

One way to break degeneracies between models is to measure the clustering strength of galaxies, so as to relate them to the dark matter halos they reside in. Observationally, galaxy clustering is usually quantified via the (angular) two-point correlation function (2PCF). This has been measured in the local Universe and at low redshifts from large ground-based surveys (e.g. Norberg et al. 2002; Budavári et al. 2003; Zehavi et al. 2005; Li et al. 2006), and later out to $z \sim 1$ (e.g. Meneux et al. 2009), $z \sim 2$ (e.g. Blanc et al. 2008; Wake et al. 2011; Lin et al. 2012; McCracken et al. 2015), and $z \sim 3 - 8$ (e.g. Hildebrandt et al. 2009; Barone-Nugent et al. 2014; Harikane et al. 2016; Ishikawa et al. 2017; Harikane et al. 2018; Ye et al. 2025). Recent works based on JWST imaging data have extended measurements of the 2PCF out to $z \sim 11$ (Dalmasso et al. 2024) and $z \sim 12$ (Paqueau et al. 2025) with photometric redshifts informed by deep NIRCam imaging, or made use of NIRCam/grism surveys providing spectroscopic redshifts out to $z \sim 8$ (Shuntov et al. 2025).

On the other hand, the clustering behavior of dark matter halos is relatively well understood based on cosmological N-body simulations (e.g. Springel et al. 2005), and analytical models (e.g. Cooray & Sheth 2002). Combining this with a so-called halo occupation distribution (HOD; e.g. Berlind & Weinberg 2002), one can then relate halos to galaxies, and model the galaxy 2PCF. A quantity that is used to characterize the clustering of halos is the so-called halo bias which is defined as the excess clustering of halos relative to the matter density field. Analogously, the galaxy bias is defined as the excess clustering of galaxies relative to the matter density field as a function of the physical scale r ,

$$b_g^2(r) = \frac{\xi_{gg}(r)}{\xi_{\text{DM}}(r)} \quad (1)$$

where ξ_{gg} is the galaxy-galaxy 2PCF, and ξ_{DM} is the 2PCF of the matter density field. As already shown by Mo & White (1996), the halo bias and thus the galaxy bias is scale-independent on large scales where it is only a function of the halo mass. This bias is referred to as the linear bias because it is valid in the linear regime, where fluctuations in the matter field can be approximated as linear deviations from the mean density of the Universe. Given a measurement of the 2PCF, one can fit for the parameters of the HOD and infer the galaxy bias as a number-weighted average of the linear halo bias (see e.g. Paquereau et al. 2025).

Clustering of halos and galaxies is stronger on smaller scales, also referred to as the non-linear regime, where the (non-linear) physics of the collapse of halos into virialized structures, and of galaxy formation become important. Various works show that non-linear effects still enhance the clustering of halos on relatively large, so-called quasi-linear scales (see e.g. Jose et al. 2016 and references therein). Building on their results for halos, Jose et al. (2017) investigated the clustering of Lyman break galaxies (LBGs) at $z = 3 - 5$ and found that on angular scales of $\sim 5 - 100''$ their clustering is enhanced by an order of magnitude due to non-linear effects.

Robertson (2010) suggested that the galaxy bias of high redshift LBGs could be constrained from measurements of cosmic variance, designated as σ_{CV} hereafter. They define a galaxy bias as

$$b_{g, \text{CV}} = \frac{\sigma_{\text{CV}}}{\sigma_{\text{DM}}} \quad (2)$$

where σ_{DM} is the field-to-field variance in the underlying dark matter density field. Equation 2 has been successfully applied in the literature to measure the bias for galaxies of different types out to $z \sim 2$ (López-Sanjuan et al. 2015; Cameron et al. 2019). As discussed in López-Sanjuan et al. (2015), this bias inferred from σ_{CV} combines clustering on all scales smaller than the probed survey volume, including non-linear scales.

In this work, we use the sample of LBGs compiled in W25 to measure σ_{CV} for UV-bright galaxies at $z \sim 10$. This can be related to the clustering strength of these galaxies through Equation 2, which can in turn break degeneracies between different models that have been proposed to explain the high abundance of UV-bright galaxies at $z \sim 10$. The paper is structured as follows:

We present the data as well as the methods applied to measure cosmic variance in Section 2. Our results are presented in Section 3, starting with the measurements of σ_{CV} . We then describe our implementation of

various simple models that boost the number density of UV-bright galaxies at $z \sim 10$ in the `UniverseMachine`, and investigate their impact on σ_{CV} . This is followed by a discussion of our results in Section 4 which includes a quantification of the effect of non-linear scales on the measured σ_{CV} , and future prospects for σ_{CV} constraints based on additional pure parallel imaging. We summarize our findings and conclude in Section 5.

Throughout this work we assume a Λ CDM cosmology with parameters from the nine-year Wilkinson Microwave Anisotropy Probe Observations (Hinshaw et al. 2013), $h = 0.6932$ and $\Omega_{m,0} = 0.2865$. All magnitudes are reported in the AB system (Oke & Gunn 1983).

2. DATA AND METHODS

The data used in this work are largely identical to the data described in W25. We provide a brief summary below, and refer the reader to W25 for details.

2.1. Imaging and Photometry

This work builds on JWST and HST imaging mosaics from various legacy surveys, retrieved from the DAWN JWST Archive (DJA¹), as well as pure parallel imaging from the first PANORAMIC data release² (Williams et al. 2025). All of these mosaics have been reduced with `grizli` (Brammer 2023), as described in e.g. Valentino et al. (2023). A list of all JWST programs contributing imaging data to the legacy fields is provided in Section 2.1 of W25.

Photometric catalogs are generated following the methods outlined in Weibel et al. (2024) and Williams et al. (2025). We detect sources in an inverse-variance weighted stack of the NIRCam/LW filters F277W, F356W, and F444W using `SourceExtractor` (Bertin & Arnouts 1996). Running `SourceExtractor` in dual mode, we measure fluxes on point spread function (PSF) matched versions of the mosaics in each filter through circular apertures with a radius of $0.16''$, and scale these fluxes to total based on the Kron aperture in the detection image, and an additional correction to account for flux in the wings of the PSF (see e.g., Skelton et al. 2014; Whitaker et al. 2019; Weaver et al. 2024).

2.2. Galaxy Sample

W25 selected LBGs as F115W, F150W, and F200W dropouts corresponding to $z \sim 10$, $z \sim 13$, and $z \sim 17$. We only use the F115W dropout sample here which consists of 86 galaxies at $z \sim 10$. The sample selection mostly relies on conservative color cuts defined as

¹ <https://dawn-cph.github.io/dja/imaging/v7/>

² <https://panoramic-jwst.github.io/>

$$\begin{aligned}
& \text{F115W} - \text{F150W} > 1.5 \wedge \\
& \text{F150W} - \text{F356W} < 0.5 \wedge \quad (3) \\
& \text{SNR}(\text{F150W}) > 8 \wedge \\
& \text{SNR}(\text{F200W}) > 3
\end{aligned}$$

where FXXXW is the AB-magnitude in each filter, and we apply a 2σ upper limit to the flux in F115W before computing the first color. This selection is complemented with the `use_phot` flag from [Weibel et al. \(2024\)](#). We further reject confident low redshift interlopers based on `eazy` ([Brammer et al. 2008](#)), and perform a visual inspection to remove remaining diffraction spikes, spurious detections, and sources with clear detected flux below the supposed Lyman break. We exclude data from the Abell-2744 cluster field in this work to avoid complications introduced to flux limits and volumes by gravitational lensing, which reduces the sample size to 74 galaxies.

Of these 74 galaxies, 18 have publicly available spectroscopic redshifts on the DJA. Reassuringly, all of them are confirmed to be at $z > 9$. As discussed in Section 2.5 of [W25](#), while spectroscopic redshifts are preferentially available for sources in legacy fields with deep photometry in many bands, the 100% success rate of the selection for sources with z_{spec} nevertheless suggests a high purity of the sample.

All galaxies are initially fit with `eazy`, fixing the redshift to the nominal range of the dropout selection plus (minus) 0.1 at the upper (lower) end, $z \in (8.5, 11.4)$. To consistently infer the final redshift, UV-magnitude M_{UV} , and -slope β for each source within a Bayesian framework, we run `bagpipes` ([Carnall et al. 2018](#)), fixing the redshift to $z = z_{\text{eazy}}$, with a Gaussian prior whose width is determined by half the difference between the 84th and the 16th percentile of the `eazy` fit. We then sample 500 SEDs from the `bagpipes` posterior, and measure z , M_{UV} , and β from each to get our final estimates and uncertainties of these quantities as the median, 16th and 84th percentiles.

2.3. Completeness Correction

Again following [W25](#), we determine the completeness of the sample in two steps. First, we assess the detection completeness as a function of the source magnitude in the detection image through injection-recovery simulations with the GaLAXy survey Completeness AlgoRithm 2 (GLACiAR2) software ([Carrasco et al. 2018; Leethochawalit et al. 2022](#)). Second, we estimate the selection completeness by creating mock SEDs based

on the redshift and UV-properties from the 500 SEDs sampled from the `bagpipes` posterior. For each of the 500 sets of z , M_{UV} , and β , we produce a mock SED with a power-law shape, and create 1000 realizations of the photometry by adding Gaussian scatter to the synthetic flux in each band according to the flux uncertainties specified in the photometric catalog. The selection completeness is then given by the number of the 1000 realizations that would pass the selection cut in [Equation 2.2](#), divided by the number that would be detected by `SourceExtractor`, according to the combined SNR in F277W, F356W, and F444W. In this way, the two completeness values are independent and can be multiplied to obtain a total completeness for each source. We further convert the values in the weight maps from the DJA to an M_{UV} limit per pixel following [W25](#), and derive a median M_{UV} limit per field.

2.4. Cosmic Variance Measurements

We follow two different approaches to empirically constrain cosmic variance at $z \sim 10$: bootstrapping and Bayesian forward modeling. We start from PANORAMIC pointings outside of any legacy fields with > 2 deg separation on the sky, so that they can be considered uncorrelated in terms of galaxy clustering³. There are 28 such pointings, most of which consist of a single NIRCam field of view (see [Williams et al. 2025](#)). To include the legacy fields as additional lines of sight without accounting for the more complex survey geometries and substantially larger area per field, we create “mock” NIRCam pointings by placing the NIRCam field of view at a random position and with a random position angle on top of each legacy field mosaic. We assert that at least 90% of the footprint are covered by data in all required filters (see [Section 2.2](#)) and then treat the sampled part of the legacy field as an independent field. We proceed in this way for the UDS, COSMOS, EGS, and the two GOODS fields (North and South). The NEP-TDF consists of a single NIRCam pointing and can therefore be included as is. This yields 34 independent lines of sight in total, with roughly identical survey geometries, i.e. single NIRCam pointings of $\sim 9.7 \text{ arcmin}^2$.

Next, we wish to quantify the cosmic variance for different M_{UV} limits. For a given limit, we include only brighter galaxies and restrict the analysis to fields with sufficient median depth. Consequently, the number of

³ We choose this somewhat arbitrary scale to be roughly twice the angular BAO scale at $z \sim 10$. At these scales, any bias incurred from large-scale density modes will be at the percent-level, much below our sensitivity.

contributing fields decreases toward fainter limits, while the number of galaxies decreases toward brighter limits. Given these constraints, we adopt $M_{UV} < -19.5, -20$, and -20.5 as feasible limits, corresponding to 9, 17, and 29 independent fields, and 57, 37, and 19 galaxies respectively. To account for remaining small differences in the survey area of different fields, we scale the observed number of galaxies in each field to the nominal NIRCam field of view of 9.7 arcmin².

2.4.1. Bootstrapping

The field-to-field variance in the number counts comes from the combined effect of Poisson noise and cosmic variance. To separate out the latter, we use the relation

$$\sigma_{CV}^2 = \frac{\sigma_{\text{total}}^2 - \sigma_{\text{Poisson}}^2}{\mu^2} = \frac{\langle N^2 \rangle - \langle N \rangle^2 - \langle N \rangle}{\langle N \rangle^2} \quad (4)$$

following e.g. Somerville et al. (2004) and Moster et al. (2011) where N stands for the completeness corrected galaxy number counts per field, $\mu = \langle N \rangle$ is the mean number count, and we make use of the fact that the Poisson contribution to the variance is $\sigma_{\text{Poisson}}^2 = \langle N \rangle$. Note that σ_{CV} is defined as a fractional variance.

Equation 4 can be directly applied to the numbers of galaxies per field for the three M_{UV} limits respectively. To estimate uncertainties for the inferred cosmic variance, we perform 1000 bootstrapped measurements of σ_{CV} by sampling 34 of the 34 fields each time, allowing for fields to be sampled multiple times. To additionally leverage the larger survey area covered by the legacy fields (CEERS, COSMOS, UDS, GOODS-N, and GOODS-S), we sample a new random NIRCam pointing within each field’s footprint in each iteration. We then take the median as well as the 16th and 84th percentile of the 1000 measurements as our final bootstrapped values and uncertainties for σ_{CV} .

2.4.2. MCMC-Fitting

A more principled approach for quantifying the cosmic variance is to directly fit to the galaxy number count distribution. To this end, we model the observed distribution of completeness-corrected galaxy counts across independent fields and for our different M_{UV} limits using a Bayesian Markov Chain Monte Carlo (MCMC) framework. We assume that the underlying field-to-field distribution of galaxy counts follows a Gamma distribution (Steinhardt et al. 2021; Jespersen et al. 2025c). The Gamma distribution is characterized by a mean and a variance, which, in contrast to the Poisson distribution, can be specified independently of each other, allowing for a super-Poissonian variance. In the

limit that the variance becomes equal to the mean, the Gamma distribution closely resembles the Poisson distribution. Therefore, the Gamma distribution, with variance equal to $\sigma_{\text{Poisson}}^2 + \mu^2 \sigma_{CV}^2$ goes towards the expected Poisson distribution in the limit of no cosmic variance/clustering, with the σ_{CV} -term encoding exactly the cosmic variance/clustering we wish to constrain.⁴. Other distributions, such as the negative binomial distribution, are also possible adequate choices since they also share the same characteristic — Poisson-like in the absence of cosmic variance, but allowing for the inclusion of cosmic variance. However, the difference between adopting either the Gamma or Negative Binomial is empirically negligible (Jespersen et al. 2025c).

We infer the mean and variance parameters⁵ of the Gamma distribution via MCMC sampling using the `emcee` sampler (Foreman-Mackey et al. 2013). Critically, the likelihood function we adopt down-weights variance contributions from rare, highly over-dense fields. This is achieved by defining the likelihood as the Negative Binomial distribution across the binned number counts, which in essence acts as an outlier-resistant Poisson-likelihood, as per the recommendation (and typical best-practice approach) of Hogg et al. (2010). This approach reduces the influence of outlier fields, in line with the findings of Jespersen et al. (2025c), who find that empirically calibrated cosmic variances are biased towards high values. This is due to the highly skewed nature of the distribution of galaxy number counts across different fields.⁶ We adopt the maximally non-informative prior distribution for the variance ($p(\sigma) \propto \sigma^{-1}$, also known as the *Jeffrey’s prior*), which effectively forces the variance to be small unless a high variance is strongly favored by the data (Jeffreys 1946). We also adopt a weak Gaussian prior for the mean, centered on the sample mean and with a width of 30% of the sample mean. This mainly helps guide the sampler and does not have any meaningful effect on our inference results.

In addition to the real data, we apply the same measurement to galaxies in the `UniverseMachine` (Behroozi et al. 2019), a parametric empirical model built with a

⁴ Another way to think of the Gamma distribution is as the distribution arising from the theoretical expectation for positive-definite variables (galaxy counts) with stochastic large-scale structure modulation.

⁵ In practice, the input parameters to the Gamma distribution are a shape and a scale parameter, but these are directly related to the mean and variance, making their use in inference equivalent.

⁶ To clarify, the skewness implies that the galaxy number count distribution is highly asymmetric, having a preference for both very small and very large values, depopulating the central region that usually stabilizes fits.

set of differential equations governing galaxy evolution on pre-computed merger trees from the Bolshoi-Planck dark matter simulation (Klypin et al. 2016; Rodríguez-Puebla et al. 2016). It provides eight independent mock light-cones for the survey geometries of the five CANDELS fields (Grogin et al. 2011). We use four out of the five, since one has unexplainable and significantly lower typical number densities, giving us access to 32 independent “lines of sight” of area typically a bit below a square degree. Further, the **UniverseMachine** was directly calibrated on observational constraints, including cross-correlation functions at $0 \leq z \leq 0.13$, auto-correlation functions at $z \leq 0.7$, stellar mass functions out to $z \sim 8$, as well as cosmic star formation rate densities and UVLFs out to $z \sim 10$.

We measure the mean number of galaxies and their variance for the different M_{UV} limits within light cones in the **UniverseMachine** whose size is given by the size of a NIRCam pointing on the sky and extends over $9.2 < z < 10.9$. This is slightly smaller than the nominal redshift range of the F115W dropout bin ($8.6 < z < 11.3$, see W25) to approximate the redshift selection function which declines towards the edges of the nominal range. We emphasize that the resulting cosmic variance includes contributions from clustering on all scales smaller than the survey volume, including non-linear scales. Thanks to the consistent measurement method, we can however directly compare the values inferred from the **UniverseMachine** to those inferred from the data. We integrate the dark matter power spectrum over the same survey volume, to estimate the variance in the underlying dark matter distribution using a python version of the code **QUICKCV** (Newman & Moster 2014), described in Newman & Davis (2002), to obtain $\sigma_{\text{DM}} = 0.031$. With this, we can turn our estimated values of σ_{CV} into estimates of the (cosmic variance based) galaxy bias $b_{g,\text{CV}}$ using Equation 2. We note that a slight increase or decrease in the assumed redshift range that is used to approximate the LBG selection function does not have a critical impact on σ_{DM} . For example, assuming the maximal nominal range, $8.6 < z < 11.3$ yields $\sigma_{\text{DM},\text{min}} = 0.025$, while a narrower range of $9.3 < z < 10.3$ yields $\sigma_{\text{DM},\text{max}} = 0.039$, reflecting changes of $< 30\%$.

3. RESULTS

3.1. Observational Constraints

We start by presenting our observational constraints on cosmic variance, and the implied galaxy bias, both from bootstrapping Equation 4, and the MCMC-fitting approach.

3.1.1. Bootstrapping

From our 1000 bootstrapped samples we find the following values for the three M_{UV} limits: $\sigma_{\text{CV,bootstr.}} = 0.96^{+0.28}_{-0.26}$, $1.76^{+0.50}_{-0.43}$, and $2.37^{+0.64}_{-0.44}$. As discussed in Section 2.4.2, the underlying number count distributions are highly skewed, and truncated at 0 which implies that the measured variance is likely biased high. This effect is more significant for small number counts, and if the intrinsic (cosmic) variance is higher, as is expected for more massive galaxies. In other words, if UV-bright galaxies at $z \sim 10$ are strongly clustered, the expected intrinsic distribution of number counts per NIRCam pointing will have a long tail out to high number counts. Any measurement of the variance of that distribution based on small number statistics is therefore expected to be biased high due to a small number of outliers boosting the variance (see Jespersen et al. 2025c). A test on how much this affects the cosmic variance values inferred through bootstrapping is provided by our second approach to measuring σ_{CV} .

3.1.2. MCMC Fitting

MCMC fitting of a Gamma distribution to the measured number counts per field yields $\sigma_{\text{CV}} = 0.96^{+0.20}_{-0.18}$, $1.46^{+0.54}_{-0.44}$, $1.71^{+0.72}_{-0.59}$, for $M_{\text{UV}} < -19.5$, -20 , and -20.5 , and we subsequently take these as our fiducial values. They are lower than those inferred from the bootstrapping above for the two brighter bins, but consistent within the 1σ uncertainties. This meets our expectation that the bootstrapped values are biased high in a regime of strong clustering and low number statistics. While this effect may also have an impact on the values inferred through MCMC-fitting, it is to some degree mitigated by our prior and likelihood choice, which forces the variance to be small unless the data strongly prefers it (see Section 2.4.2). The raw posterior samples of the mean, standard deviation, and inferred σ_{CV} are shown in Figure 8 in Appendix A.

In Figure 1, we show the cosmic variance values inferred with the two different methods and for the three M_{UV} limits, and compare them to values from the **UniverseMachine**, measured using the MCMC-fitting approach. The secondary y-axis represents the cosmic variance inferred galaxy bias as defined in Equation 2. The values from the **UniverseMachine** agree well with our measurements. Given that they are measured in a consistent way, this indicates that the clustering of UV-bright galaxies at $z \sim 10$ in the **UniverseMachine** is realistic, and that it was reasonable to calibrate σ_{CV} to it in W25. We note that at the same time, the **UniverseMachine** under-predicts the abundance of UV-

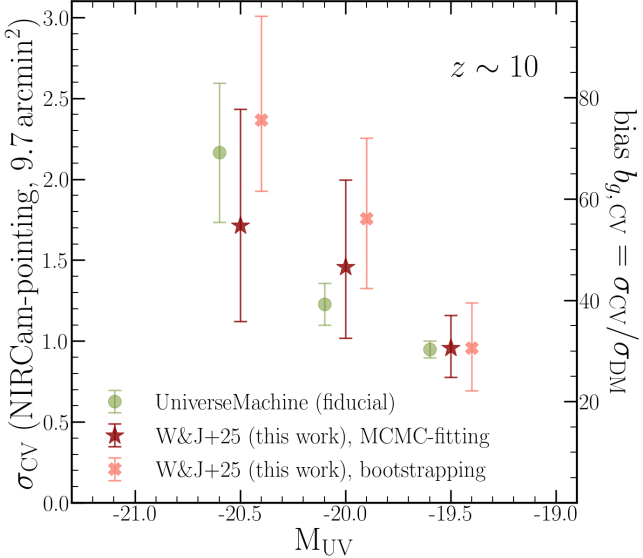


Figure 1. Cosmic variance σ_{CV} in the galaxy number count at $z \sim 10$ for a NIRCam pointing sized survey (9.7 arcmin^2). We plot values inferred through two different methods: bootstrapping Equation 4 over 34 independent fields (crosses), and MCMC-fitting to the distribution of number counts per field (stars). The secondary y-axis shows the galaxy bias inferred by cosmic variance, as defined in Equation 2. Measurements are shown for three M_{UV} limits, $M_{\text{UV}} < -19.5$, -20 , and -20.5 with different markers being slightly displaced on the x-axis for better visual separation. For comparison, we show values extracted using the same MCMC-fitting method from the **UniverseMachine** (green dots).

bright galaxies at $z \sim 10$ by a factor $\gtrsim 5$ and further discuss the implications of this in Section 3.2.

Our measured values of σ_{CV} imply that cosmic variance has a large impact on the uncertainty in the number counts of UV-bright galaxies at $z \sim 10$. For example, at $M_{\text{UV}} < -20.5$, we measure $\sigma_{\text{CV}} = 1.71_{-0.59}^{+0.72}$, suggesting that the cosmic variance driven fractional uncertainty in the galaxy number count inferred from a single NIRCam pointing is as high as $\sim 110\text{--}240\%$. Given that the Poisson contribution to the uncertainty is $\sim \sqrt{N}$, this means that cosmic variance dominates the uncertainty in the number count by far in this case. The impact of cosmic variance scales with the number of independent fields as $\sigma_{\text{CV}} \propto 1/\sqrt{N_{\text{fields}}}$, and it also decreases for larger field sizes as we will quantify in Section 4.1.

3.2. Model Comparison

Our measurements of cosmic variance and thus the clustering strength of LBGs at $z \sim 10$ put complementary constraints on galaxy physics at cosmic dawn. The **UniverseMachine** reproduces the cosmic variance we measure (see Figure 1), but it under-predicts the number density of UV-bright galaxies (i.e. the mean number

of galaxies per NIRCam pointing) at $z \sim 10$ by a factor of 4.9 ± 0.8 , 5.3 ± 1.2 and 8.7 ± 1.9 for $M_{\text{UV}} < -19.5$, -20 , and -20.5 , corresponding to 4.8, 3.6, and 4.2σ tensions between the simulation and the data respectively. Various models have been proposed in the literature to account for the observed abundance of galaxies at $z \sim 10$. While they were all designed to reproduce the observed galaxy number density (see e.g. W25), they affect the clustering in different ways, meaning that an accurate measurement of the clustering strength can be used to distinguish between different models. As discussed and quantified in e.g. Mirocha (2020), Muñoz et al. (2023), Shen et al. (2024), and Gelli et al. (2024), this is particularly true for models invoking stochasticity in the SFH to boost galaxy number counts. Such models increase the scatter in the $M_{\text{UV}}-M_{\text{halo}}$ relation, so that observed UV-bright galaxies tend to reside in lower mass halos that have up-scattered in UV-luminosity due to an ongoing starburst. Since lower mass halos are less clustered, this decreases the clustering signal. In addition, the halos that have up-scattered in M_{UV} at a given point in time are a random sub-set of all the halos of that mass, further diluting their clustering strength.

Here, we implement different models in the **UniverseMachine** and quantify their effect on both the number density, and the cosmic variance. Our simple models represent classes of models that have been proposed in the literature as an explanation for the high abundance of UV-bright galaxies at $z \sim 10$. To facilitate comparing models throughout the paper, we assign a label consisting of a letter and a number to each of them.

Global ΔM_{UV} (A1): We boost the UV-luminosity of all galaxies in the **UniverseMachine** by ΔM_{UV} in magnitudes, without changing any other properties. This simulates a uniform decrease in the mass-to-light ratio across all galaxies, e.g. through a global change towards a more top-heavy IMF, or a lack of dust attenuation.

ΔM_{UV} for $M_{\text{halo}} > X$ (A2): Instead of boosting the UV-luminosity of all galaxies, we only boost it for galaxies residing in halos with $\log(M_{\text{halo}}/\text{M}_\odot) > 10$, and > 10.5 . This simulates the effect of e.g. AGN boosting the UV-luminosity of galaxies that reside in massive halos.

Global SFE (B1): We model a constant SFE across all galaxies in the **UniverseMachine**, where $\text{SFE} = M_*/(f_b M_{\text{halo}})$ and $f_b = 0.16$ is the baryon fraction, and then continuously increase SFE to boost the number of UV-bright galaxies. In contrast

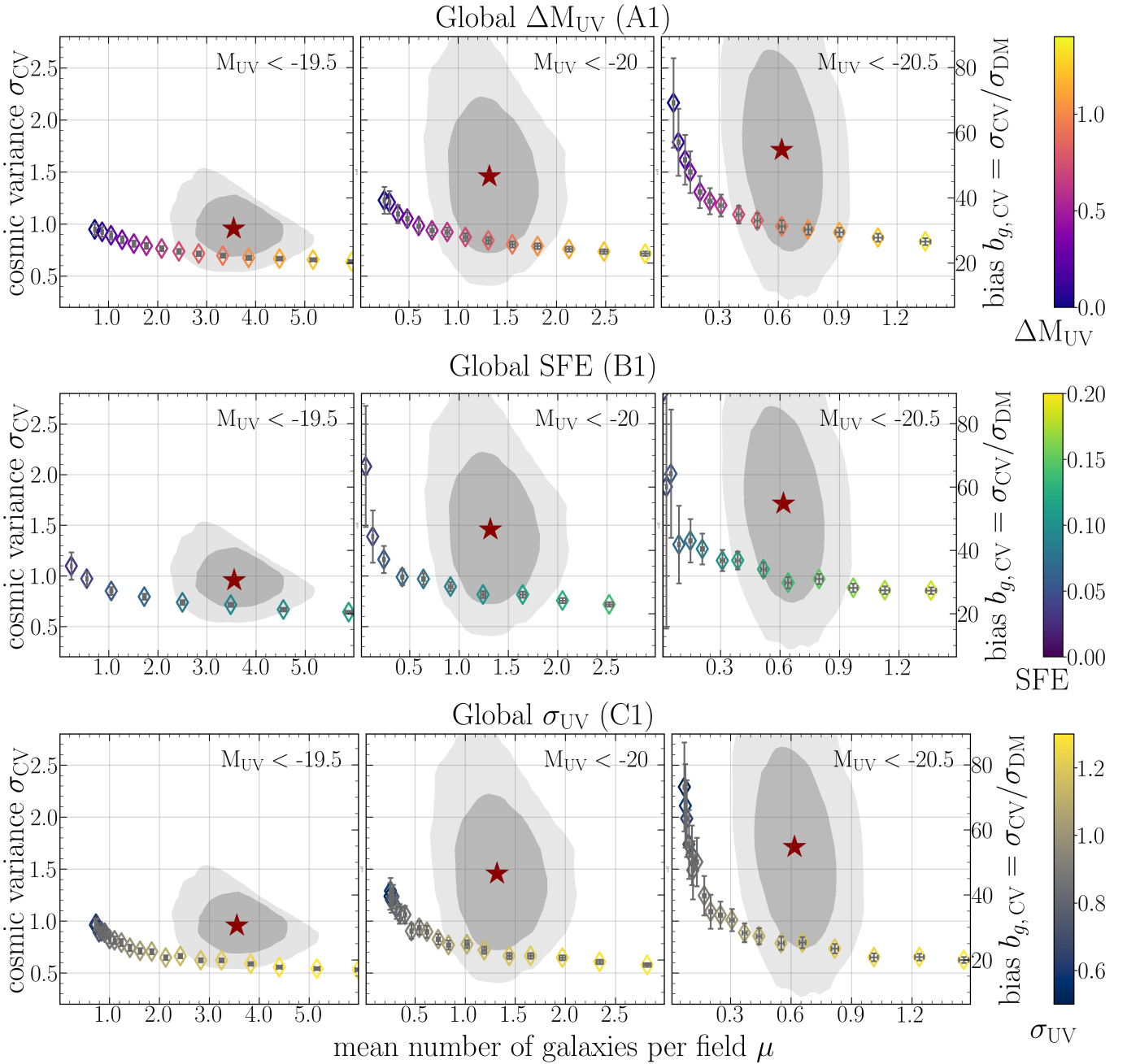


Figure 2. Combined constraints on the abundance of galaxies at $z \sim 10$, quantified as the mean number of galaxies per field (i.e. per NIRCam pointing), μ , and their clustering, quantified by the cosmic variance σ_{CV} . Each row of panels corresponds to a simple model implemented in the `UniverseMachine` to represent a class of models invoked to explain the abundance of UV-bright galaxies at $z \sim 10$. From left to right, panels correspond to different M_{UV} limits as indicated in the top row of panels. The red stars and gray contours show our measurements, and the 1, and 2σ confidence regions obtained through MCMC-fitting. We plot different realizations of each model by gradually increasing the quantity of interest: ΔM_{UV} , the boost to the UV-luminosity of all galaxies (in mag); the SFE (defined as $M_*/(f_b M_{\text{halo}})$); and σ_{UV} , the scatter in the $M_{\text{UV}}-M_{\text{halo}}$ relation (in mag). This illustrates that different models follow similar tracks on the $\sigma_{\text{CV}}-\mu$ -plane, showing an inverse relationship between μ and σ_{CV} . Models can however be distinguished by considering different M_{UV} limits simultaneously (see Section 3.3).

to the boost in M_{UV} , this model starts from M_{halo} in the **UniverseMachine** which we convert to $M_* = \text{SFE} f_b M_{\text{halo}}$. M_* is then converted to M_{UV} , assuming the typical M_* - M_{UV} -relation in the **UniverseMachine**, including scatter.

DMSFE: $\text{SFE} \propto M_{\text{halo}}^q$ (B2): Building on the previous model, we implement a power-law scaling of the SFE with M_{halo} with a non-zero slope, $\text{SFE} \propto M_{\text{halo}}^{0.5}$, similar to the density modulated SFE (DMSFE) scenario proposed by [Somerville et al. \(2025\)](#). To explore the impact of the slope of this scaling law, we also test a model with a sharper scaling, $\text{SFE} \propto M_{\text{halo}}^{0.6}$. In both cases, we continuously increase the normalization of the relation as $\text{SFE}_{\text{peak}} = \text{SFE}(M_{\text{halo}} = 10^{11.6} M_\odot)$, the SFE at the maximum halo mass in the **UniverseMachine**.

Global σ_{UV} (C1): To mimic the effect of enhanced stochasticity in the star formation, we increase the global scatter in the $M_{\text{UV}}-M_{\text{halo}}$ relation, denoted as σ_{UV} . It is important to note that σ_{UV} cannot be uniquely related to stochasticity in the SFHs of galaxies. Other processes that contribute to σ_{UV} are variations in the metallicity, dust attenuation, IMF, SFE, or the nebular contribution to the UV-continuum.

M_{halo} -dependent σ_{UV} (C2): Finally, we implement a scaling of σ_{UV} with M_{halo} following [Sun et al. \(2023\)](#), $\sigma_{\text{UV}} = \sigma_{\text{UV, norm}} - 1/3 \log(M_{\text{halo}}/10^{10} M_\odot)$, where $\sigma_{\text{UV, norm}} = \sigma_{\text{UV}}(M_{\text{halo}} = 10^{10} M_\odot)$.

For each model, we create multiple realizations, gradually increasing the quantity of interest (ΔM_{UV} , SFE, SFE_{peak} , σ_{UV} , and $\sigma_{\text{UV, norm}}$ respectively), and apply the MCMC-fitting explained in Section 2.4.2 to infer the mean number of galaxies per field μ , and σ_{CV} . We present the resulting combined constraints on the abundance and the cosmic variance in Figures 2 and 3. Each set of three panels represents our three M_{UV} limits. The contours show the 1σ and 2σ confidence regions of the MCMC-fitting to the data from Section 3.1.2 (identical to the bottom left panels in Figure 8).

3.2.1. General Observations

The tracks that the different models describe on the $\sigma_{\text{CV}}-\mu$ plane look overall similar as they show the same qualitative trend of decreasing σ_{CV} for higher μ . This is because all models increase the normalization of the $M_{\text{UV}}-M_{\text{halo}}$ relation such that at fixed halo mass, galaxies have a higher UV-luminosity. Conversely, this means that galaxies at fixed M_{UV} reside in lower mass halos which are less clustered. This is true for any model

that increases the number density of UV-bright galaxies without changing the properties of the underlying dark matter halos. In order to increase the number of bright galaxies, they have to reside in halos that are more abundant, i.e. in halos of lower mass. As a consequence, none of the explored models is capable of exactly reproducing our combined measurements of the abundance and the clustering strength shown by a red star in Figures 2 and 3. We quantify the statistical significance of the resulting tension in Section 3.3, but note here that it may also indicate that our measurements are still biased high due to the reasons outlined in Section 3.1.1 (see also [Jespersen et al. 2025c](#)).

While the different models show a qualitatively similar behavior, they differ in their detailed quantitative predictions. For example, models that increase σ_{UV} decrease σ_{CV} most significantly for all M_{UV} limits. It is further important to note that in order for a model to successfully reproduce our measurements, it has to match the constraints for all three M_{UV} limits simultaneously (see Section 3.3). Subsequently, we discuss the different models shown in Figures 2 and 3.

3.2.2. Models Changing Global Properties

We start with the models in Figure 2: a global boost in M_{UV} (model A1), a global increase in the SFE (B1), and enhanced scatter in the $M_{\text{UV}}-M_{\text{halo}}$ relation, independent of halo mass (C1). Boosting the UV-luminosity of all galaxies by $\Delta M_{\text{UV}} \sim 1$ mag matches the number density constraints in all three panels, while the implied σ_{CV} is marginally consistent with our measurements within 1σ respectively. The same is true for a model with $\sigma_{\text{UV}} \sim 1.2$, although slightly more scatter is required to match the higher number density at $M_{\text{UV}} < -19.5$, and the respective models are all inconsistent with measurements at $\gtrsim 1\sigma$ significance. The constant SFE model in turn struggles to reproduce the number densities for all three M_{UV} limits simultaneously. At $M_{\text{UV}} < -19.5$, an SFE of ~ 0.1 is favored by the data, and a higher SFE quickly over-produces the number density of galaxies. However, an SFE of $\gtrsim 0.15$ is needed to match the measured number density of $M_{\text{UV}} < -20.5$ galaxies.

3.2.3. Mass-Dependent Models

Recently proposed models to explain the observed galaxy abundance at $z \sim 10$ often go beyond changing galaxy properties globally. They instead suggest a dependence of the SFE, σ_{UV} , or the change in mass-to-light ratio on other physical properties. In Figure 3, we first show the model where we only boost M_{UV} for galaxies residing in halos above two different threshold halo masses (model A2). For a mass threshold of $\log(M_{\text{halo}}/M_\odot) > 10$, this only marginally increases the

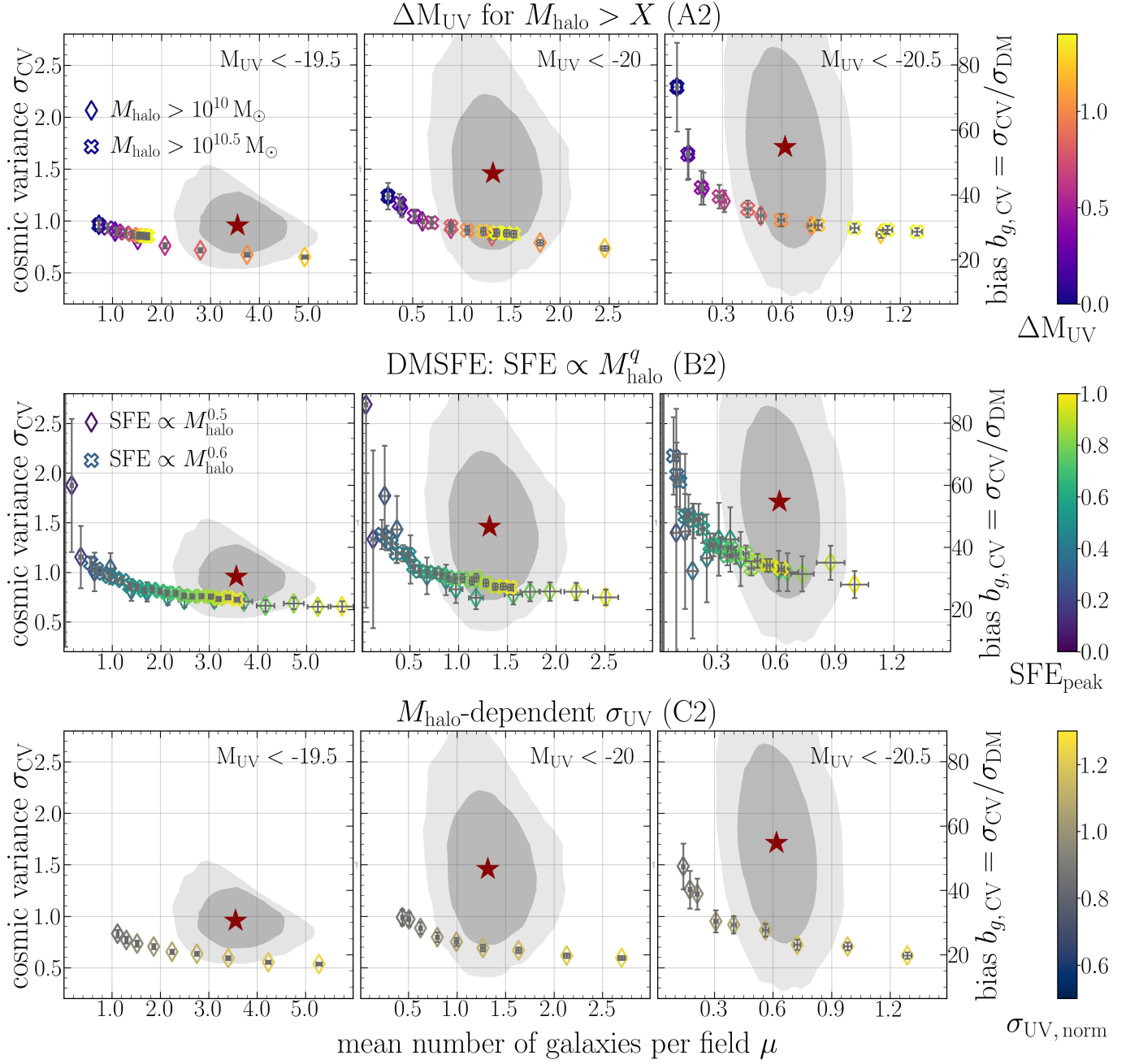


Figure 3. Same as Figure 2, but for three models where the model parameters depend on halo mass. In the first one (top, A2), the UV-luminosity is boosted by ΔM_{UV} in halos above a threshold mass. If the threshold mass is low enough ($10^{10} M_{\odot}$ or lower), this produces results that are nearly identical to a global boost (Figure 2, A1). If the threshold mass is higher ($> 10^{10.5} M_{\odot}$), there are not enough halos of that mass to reproduce the measured number density of $M_{\text{UV}} < -19.5$ galaxies. The second model (middle, B2) implements two power-law scalings of the SFE with halo mass, assuming two different slopes (0.5 and 0.6), akin to the density modulated SFE scenario from Somerville et al. (2025). Both produce models consistent with the data within 1σ , with the steeper slope implying a higher SFE_{peak} . The third model (bottom, C2) shows a scaling of σ_{UV} with $\log(M_{\text{halo}})$, following Sun et al. (2023). Similar to the global increase in σ_{UV} , this is inconsistent with the data at $> 1\sigma$ for each M_{UV} limit individually.

cosmic variance at fixed mean number count compared to the global boost in M_{UV} , and the same is true for any lower mass threshold. If we instead boost the UV-luminosity in halos with $\log(M_{\text{halo}}/\text{M}_\odot) > 10.5$, it is impossible to reproduce the number counts of galaxies with $M_{\text{UV}} < -19.5$ because the number density of halos above the mass threshold is too low. Further, different boosts would be required to match the constraints for $M_{\text{UV}} < -20$ and $M_{\text{UV}} < -20.5$ respectively, making this model unfeasible.

Models where the SFE shows a power-law dependence on halo mass $\text{SFE} \propto M_{\text{halo}}^q$ (B2) only marginally enhance σ_{CV} at fixed μ compared to the increase in SFE at all halo masses (B1). However, as opposed to the global increase in SFE, they lie within the 1σ contours for all three M_{UV} limits simultaneously. The sharper scaling ($\text{SFE} \propto M_{\text{halo}}^{0.6}$) provides a slightly better fit (see Section 3.3), but implies a higher peak efficiency, $\text{SFE}_{\text{peak}} \sim 0.94$. Even sharper slopes imply $\text{SFE}_{\text{peak}} > 1$ and are therefore un-physical. For reference, in the fiducial `UniverseMachine`, SFE_{peak} does not exceed 0.06.

Finally, analyzing the FIRE-2 simulation, Sun et al. (2023) found that the UV-scatter scales with halo mass because galaxies residing in lower mass halos exhibit more burstiness in their star formation. We show the model that assumes their proposed scaling in the bottom panels in Figure 3 (C2). Similar to the global increase in σ_{UV} , these models are inconsistent with our measurements at $> 1\sigma$ for all three M_{UV} limits individually. A normalization of the scaling law at $M_{\text{halo}} = 10^{10} \text{ M}_\odot$ of $\sigma_{\text{UV, norm}} \sim 1.1$ is required to match our number density constraints. We have also tested shallower and sharper scalings of σ_{UV} with $\log(M_{\text{halo}})$, adopting proportionality constants of 1/4 and 1/2, and found no significant differences in terms of the resulting σ_{CV} and μ . We specify the best-fitting model parameters for each model in Table 1 in Appendix B.

3.3. Combined Model Tension

As mentioned above, a successful model has to match the observational constraints across the different M_{UV} limits. To quantify the combined tension between each model and the data, we repeat the measurements presented in Figures 2 and 3 in distinct M_{UV} bins ($-20 < M_{\text{UV}} < -19.5$, $-20.5 < M_{\text{UV}} < -20$, and $M_{\text{UV}} < -20.5$). This is to ensure that each galaxy contributes only to one bin. In the case of M_{UV} limits, the brighter galaxies are present in multiple bins, introducing covariance between them. The distinct bins allow us to treat bins independently and compute a combined model tension m as the equivalent posterior distance in Gaussian units as $(\mu_{\text{model}} - \mu_{\text{data}})(\Sigma_{\text{model}} + \Sigma_{\text{data}})^{-1}(\mu_{\text{model}} - \mu_{\text{data}})^T$, where Σ_{model} and Σ_{data} are the covariance matrices for the data and the model constraints respectively. We show the combined model tension for all the models in Figure 4. At face value, all displayed models are at $\gtrsim 2\sigma$ tension with the data. However, as discussed in Sections 2.4.2 and 3.1.1, our measured σ_{CV} may be biased high and more data is needed to corroborate our measurements. We therefore subsequently focus on *distinguishing* between different models based on their relative tension with the data.

Specifically, we compare the tension of all models to the model that shows the best fit, which is the sharp DMSFE model (B2, $\text{SFE} \propto M_{\text{halo}}^{0.6}$). Consistent with our qualitative assessment above, the only model that is disfavored at a high ($> 4\sigma$) confidence is the one that boosts M_{UV} for $\log(M_{\text{halo}}/\text{M}_\odot) > 10.5$ (A2). Further, models that enhance the UV-scatter σ_{UV} (C1, C2) are tentatively disfavored at $\sim 2\sigma$ significance relative to the sharp DMSFE model, and a global increase in the SFE (B1) is disfavored at $> 2\sigma$. While these differences are not significant enough to draw any robust conclusions, we show in Section 4.3 that with sufficient additional imaging along independent lines of sight, this method allows for a robust distinction between different models.

4. DISCUSSION

Using a sample of LBGs at $z \sim 10$, compiled from imaging along 34 independent lines of sight in W25, we performed the first direct measurement of σ_{CV} at such high redshifts and found that the cosmic variance per NIRCam pointing is $\gtrsim 100\%$. Relating σ_{CV} to galaxy clustering, we illustrated that different models proposed to explain the abundance of UV-bright galaxies at $z \sim 10$ can, in principle, be distinguished based on combined constraints on σ_{CV} and the UVLF. Subsequently, we quantify the impact of clustering on non-linear scales on our measured σ_{CV} , and its implications for comparisons to measurements of the linear galaxy bias. We further discuss remaining caveats and future prospects for clustering measurements based on pure parallel imaging data.

4.1. Effect of Non-Linear Scales

By definition, the field-to-field variance is affected by clustering on all scales smaller than the survey volume. On small scales, the clustering of galaxies is enhanced by non-linear effects. The situation is complicated by the non-trivial survey geometry considered here. A NIRCam pointing consists of two quadratic modules at a small separation of $44''$. It can therefore be approximated by a rectangle of dimensions $4.4' \times 2.2'$. In practice, the third dimension of the survey volume is

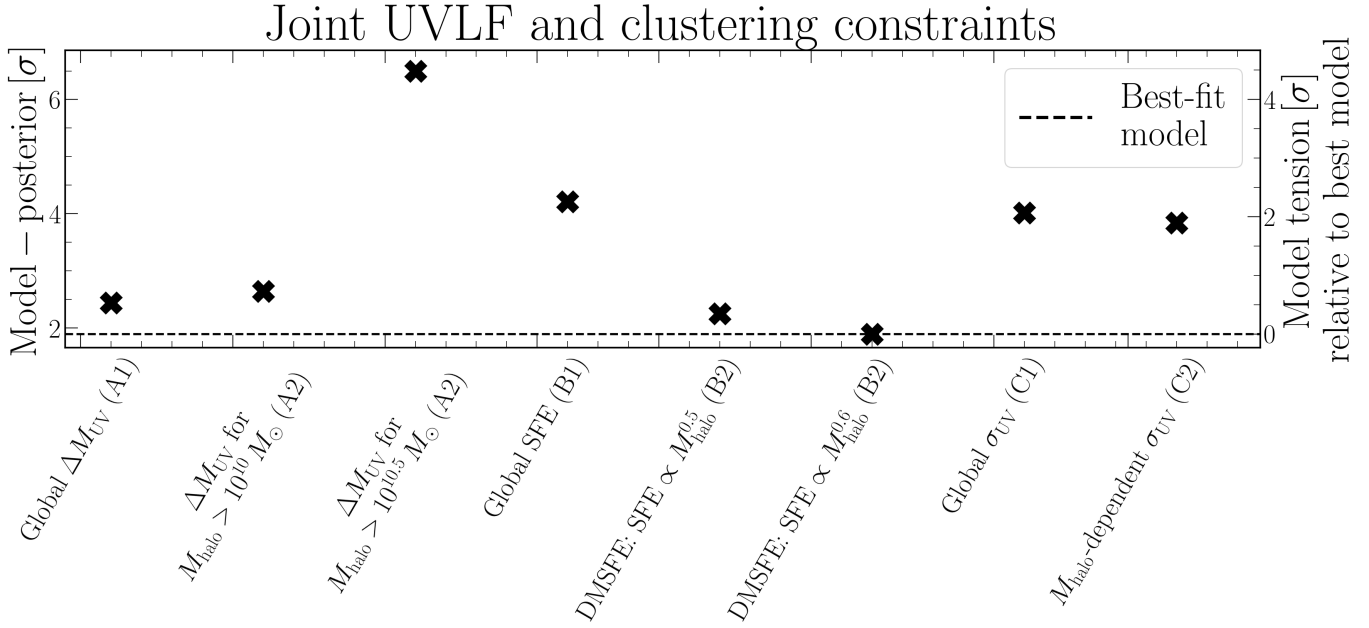


Figure 4. Combined model tension, calculated as the equivalent posterior distance in Gaussian units, across three distinct M_{UV} bins ($-20 < M_{\text{UV}} < -19.5$, $-20.5 < M_{\text{UV}} < -20$, and $M_{\text{UV}} < -20.5$), for the different models presented in Section 3.2. The secondary y-axis on the right shows the combined model tension relative to the best-fitting model (sharp DMSFE), indicated as the horizontal dashed line. This shows that models that enhance the UV-scatter σ_{UV} (bursty SF) are disfavored at $\sim 2\sigma$. The global increase in SFE is disfavored at $> 2\sigma$, consistent with our qualitative assessment in Section 3.2.2. As can be clearly seen from Figure 3, only boosting M_{UV} in halos with $M_{\text{halo}} > 10^{10.5} M_{\odot}$ cannot reproduce the measured galaxy abundance, resulting in a highly disfavored model ($\Delta\sigma > 4$).

determined by the selection function in redshift space which we approximate by a top-hat function in the range $9.2 < z < 10.9$. The resulting survey volume is a cone whose physical size is much larger in the dimension pointing away from the observer than on the sky. $4.4'$ on the sky corresponds to 1.1 pMpc at $z = 10$ while the physical distance between a galaxy at $z = 9.2$ and a galaxy at $z = 10.9$ (assuming no angular separation) is $\sim 34 \text{ pMpc}$. With this survey geometry, larger scales are therefore only sampled along a narrow cone while smaller scales are sampled in all directions.

To quantify the contribution of clustering on small, non-linear scales to the cosmic variance, (and therefore to the galaxy bias $b_{g,\text{CV}}$, measured from σ_{CV} using Equation 2), we compute $b_{g,\text{CV}}$ from the `UniverseMachine` in the same way as explained above, but for different field sizes. For comparison, we also compute the linear bias. Knowing both the halo mass, and the number of galaxies at a given M_{UV} that reside in each halo in the `UniverseMachine`, we can apply Equation (15) in Paquereau et al. (2025) to infer the linear galaxy bias as a number-weighted average of the linear halo bias from Tinker et al. (2010).

We show the results of this exercise in Figure 5 where we plot $b_{g,\text{CV}}$ as a function of the field side length for our three different M_{UV} limits, along with the scale-

independent linear bias respectively. $b_{g,\text{CV}}$ strongly increases for small field sizes, and exceeds the linear bias, driven by an increasing contribution of clustering on small, non-linear scales with the effect being stronger for brighter galaxies. At the size of a NIRCam pointing (field side length of $\sim 3.1 \text{ arcmin}$), $b_{g,\text{CV}}$ is a factor of $3 - 5$ higher than the linear bias, with a strong dependence on the M_{UV} limit (see the next Section). For field side lengths $\gtrsim 20 \text{ arcmin}$ (corresponding to physical sizes $\gtrsim 60 \text{ cMpc}$ as shown on the secondary x-axis), $b_{g,\text{CV}}$ approaches the linear bias value as the contribution of small-scale clustering becomes negligible. This is associated with larger uncertainties due to the limited size of the individual light cones in the `UniverseMachine`. Nevertheless, this illustrates the general trend of $b_{g,\text{CV}}$ with field size, and its convergence to the linear bias provided sufficiently large fields. In principle, Figure 5 can be used to convert the measured $b_{g,\text{CV}}$ to a linear bias, and compare it to inferred linear bias values in the literature, as we will do in the following.

4.2. Comparing to Measurements and Models of the Linear Bias

We use the ratio between $b_{g,\text{CV}}$ for a NIRCam pointing-sized field, and the linear bias in the `UniverseMachine` to scale our measured $b_{g,\text{CV}}$ to the

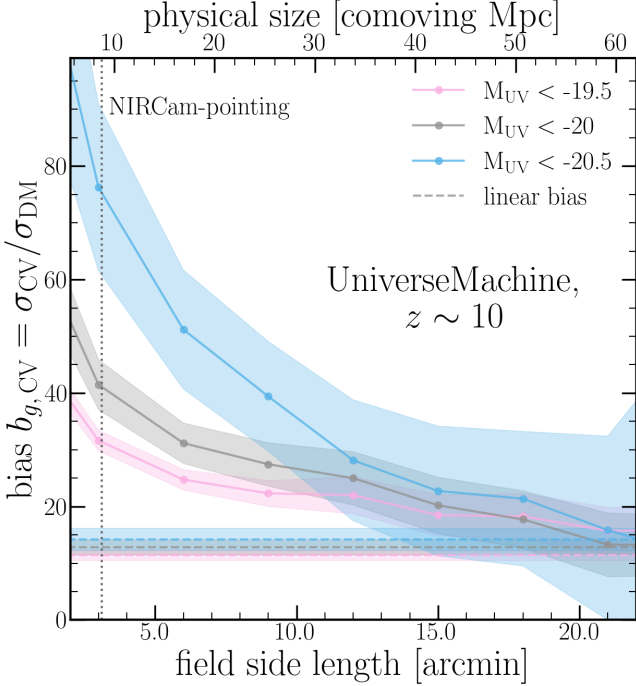


Figure 5. Galaxy bias $b_{g,CV}$, as defined in Equation 2, as a function of the field side length in arcmin for $M_{UV} < -19.5$, -20 , and -20.5 , measured from the **UniverseMachine** at $z \sim 10$. The secondary x-axis corresponds to the physical scale for the respective field side length in co-moving Mpc at $z = 10$. Linear bias values are shown as horizontal dashed lines, and the shaded regions are 1σ uncertainties respectively. This illustrates how the measured bias increases for small field sizes and exceeds the linear bias, driven by an increasing contribution from clustering on small, non-linear scales. If approximated by a square, a NIRCam pointing corresponds to a field side length of ~ 3.1 arcmin which is shown as a vertical dotted line where the bias deviates strongly from the linear value and shows a clear dependence on M_{UV} .

corresponding linear bias. For $M_{UV} < -19.5$, -20 , and -20.5 , the conversion factors can be inferred along the vertical dotted line in Figure 5 to be $2.78^{+0.28}_{-0.26}$, $3.24^{+0.49}_{-0.47}$, and $5.37^{+1.29}_{-1.27}$. Dividing our fiducial measurements of $b_{g,CV}$ by these factors, we get $b_{g,CV,corr.} = 11.0^{+2.6}_{-2.3}$, $14.4^{+5.7}_{-4.8}$, and $10.2^{+4.9}_{-4.3}$. These values are consistent with each other within 1σ , and show no obvious trend with M_{UV} .

Measurements of the linear galaxy bias at $z \sim 10$ have only become available recently. Dalmasso et al. (2024) used imaging from JADES to measure the 2PCF at $5 \leq z \leq 11$, finding linear bias values of $b_{g,lin.,D+24} = 7.2 \pm 1.5$, and 9.6 ± 1.7 for $9 < z < 10$ and $10 < z < 11$. These are somewhat lower than our corrected bias values, which may be due to their selection of galaxies with $M_{UV} < -17$, much fainter than the galaxies studied here. Paquereau et al. (2025) instead derived 2PCFs

across $0.1 < z < 12$ from COSMOS-Web data (Casey et al. 2023) above different stellar mass thresholds. Using the M_* - M_{UV} relation from Song et al. (2016), our M_{UV} limits roughly correspond to mass thresholds of $\log(M_*/M_\odot) > 8.2$, 8.5 and 8.7 . We therefore compare to their bias measurement for $\log(M_*/M_\odot) > 8.5$ which is available at $z \sim 9.25$ as $b_{g,lin.,P+25} = 10.34^{+0.69}_{-0.47}$, consistent with our corrected bias values for all three M_{UV} limits.

Gelli et al. (2024) used a simple analytical model to quantify the effect of stochastic star formation on the bias. They implemented mass dependent scatter in the M_{UV} - M_{halo} -relation following Sun et al. (2023), and computed linear bias values for different M_{UV} limits, with and without UV scatter. We consider their model for $M_{UV} < -19.5$, and the corresponding bias values at $z \sim 9.8$, which are $b_{g,lin.,G+24} = 11.73$, and $b_{g,lin.,G+24,bursty} = 9.39$. Our corrected bias value for the same M_{UV} limit of $b_{g,CV,corr.}(M_{UV} < -19.5) = 11.0^{+2.6}_{-2.3}$ is close to their value without UV-scatter, but still consistent with the bursty value, emphasizing that more data is needed to distinguish between such models.

These comparisons illustrate that using the **UniverseMachine** to factor out the effect of clustering on non-linear scales yields linear bias values consistent with measurements in the literature. While the current uncertainty in σ_{CV} is too large to allow for a distinction between different models, it is important to note that the uncertainties that are specified for linear bias measurements from fitting an HOD to the 2PCF are artificially shrunk because they are calculated within the framework of a simplified model. On the other hand, σ_{CV} provides a direct probe of the clustering of halos as well as the physical processes that determine the properties of the galaxies within them. This complicates its interpretation but it also means that σ_{CV} may have more constraining power in terms of discriminating between physical models, as we further explore below.

4.3. Future Prospects for Measurements of Cosmic Variance

The uncertainty in the measured σ_{CV} roughly scales with the square root of the available number of independent lines of sight. A substantial improvement in the bias measurement is therefore in reach with *JWST*/NIRCam pure parallel imaging, which is the perfect observing mode to acquire imaging data in random directions in the sky at very low overhead costs.

In Figure 6, we show the hypothetical 1 , and 2σ contours on the σ_{CV} - μ -plane at $M_{UV} < -20$ which we could obtain with only 50 additional lines of sight, assuming the depth distribution of the 34 fields used in this work.

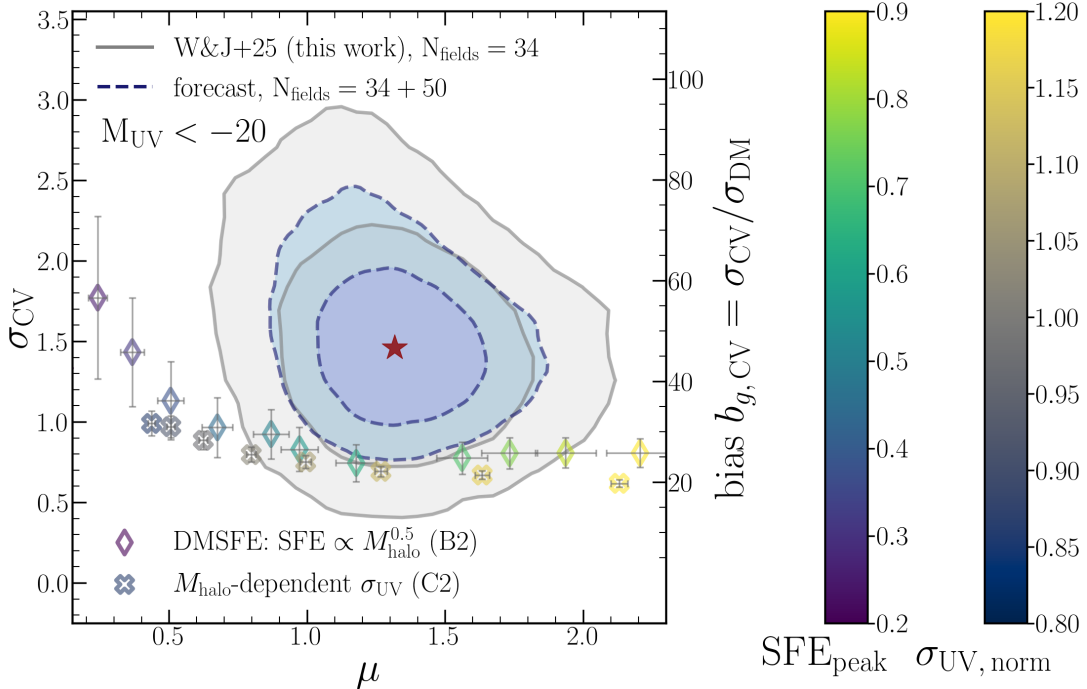


Figure 6. Combined constraints μ and σ_{CV} in analogy to Figures 2 and 3. The gray contours and red star represent our measurement in the $M_{\text{UV}} < -20$ bin. The blue contours are derived assuming that our measurements represent the ground truth and simulating the constraining power of 50 *additional* lines of sight, as could be easily obtained in a dedicated pure parallel NIRCam imaging program. The colored markers represent our models with M_{halo} -dependent UV-scatter (C2), as well as the DMSFE with $\text{SFE} \propto M_{\text{halo}}^{0.5}$ (B2). While our current constraints only disfavor such models at $\sim 1\sigma$ confidence, they could be ruled out at $> 2\sigma$ in a single M_{UV} bin with 50 additional independent NIRCam pointings.

We again plot the model with halo mass dependent UV-scatter (Sun et al. 2023, , C2), as well as the DMSFE model (Somerville et al. 2025, , B2) already shown in Figure 3. While models that match the measured μ are only disfavored at $\sim 1\sigma$ confidence with the current data, they could already be disfavored at $> 2\sigma$ confidence with 84 independent lines of sight (34 + 50). Such a data set could easily be obtained in a dedicated pure parallel imaging program in just one observational cycle, and will likely become available through a combination of parallel as well as primary imaging programs across observational cycles in the future.

To further illustrate the combined constraints that could be obtained across M_{UV} bins from such a data set, we also re-generate Figure 4 with 50 *additional* lines of sight, and show the resulting model tensions in Figure 7. In this hypothetical scenario, the models enhancing UV-scatter, globally or with an M_{h} -dependence (C1, C2), as well as the global SFE model (B1) are disfavored at $> 3\sigma$ significance, relative to the best-fitting sharp DMSFE model ($\text{SFE} \propto M_{\text{halo}}^{0.6}$, B2). The DMSFE models are more difficult to distinguish from models boosting the UV-luminosity (A1, A2) through e.g. a more top-heavy IMF, a lack of dust attenuation, or an AGN-contribution to the UV-luminosity. Nevertheless, small

differences between these models are apparent in Figure 7, and they may become statistically significant provided a much larger number of independent lines of sight.

4.4. Impact of the Completeness Correction

Our measurements of σ_{CV} and μ rely on completeness-corrected number counts. The completeness correction is outlined in Section 2.3, and in more detail in W25. One worry may be that the completeness correction artificially boosts the field-to-field variance.

To directly assess the impact of the completeness correction on our inferred cosmic variance values, we repeat the bootstrapping measurement described in Section 2.4.1 without applying the completeness correction. The resulting “raw” cosmic variance values are indeed somewhat lower than those inferred with the correction, $\sigma_{\text{CV, raw}} = 0.85^{+0.33}_{-0.35}$, $1.59^{+0.59}_{-0.61}$, and $1.95^{+0.62}_{-0.54}$ for $M_{\text{UV}} < -19.5$, -20, and -20.5. However, these values are still consistent with our fiducial values within uncertainties and they do not significantly change any of our conclusions. We further note that the completeness correction significantly boosts the inferred abundance of galaxies, consistent with a large number of literature results at $z \sim 10$, as shown in W25.

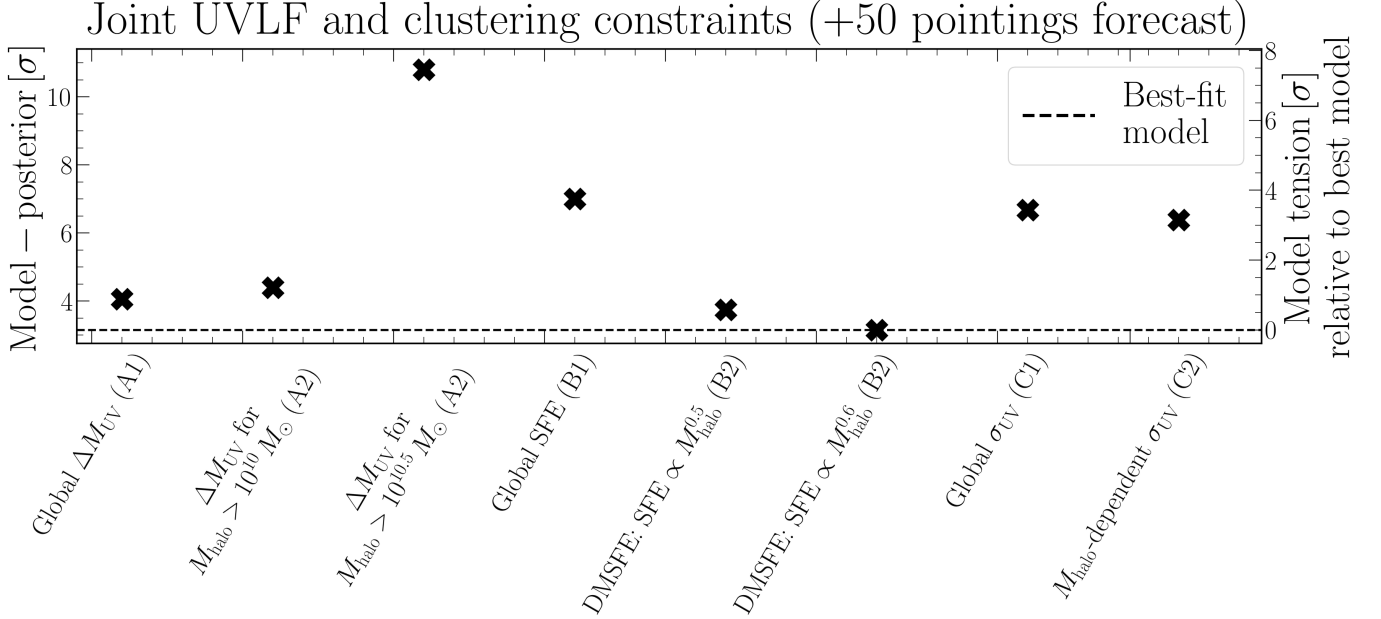


Figure 7. Same as Figure 4, but with 50 additional lines of sight following the depth distribution of the 34 fields used in this work. This shows that with only 50 additional independent NIRCam pointings, different models can be distinguished at statistically significant levels based on joint UVLF and clustering constraints. In particular, models that invoke enhanced UV-scatter (C1, C2), as well as a global increase in the SFE (B1) can be ruled out at $> 3\sigma$, relative to DMSFE models (B2), and models that boost the UV-luminosity of galaxies (A1, A2).

4.5. Reliability of Photometric Redshifts

Thus far we have illustrated the feasibility of measuring the galaxy bias for LBGs at $z \sim 10$ from a set of spatially independent NIRCam pointings, each providing imaging in at least the F115W, F150W, F200W, F277W, F356W, and F444W filters. The success of this measurement relies on robust photometric redshifts which are available at $z \sim 10$ thanks to the Lyman break shifting through the F115W filter at $z \gtrsim 8.5$. The remaining 5 or more filters then all probe the rest-frame UV, making low- z interlopers unlikely, given that the measured break is strong enough to rule out Balmer break solutions at $z \sim 2$, which is ensured by our stringent dropout selection (see Section 2.2). This is corroborated by the 100% spectroscopic confirmation rate of galaxies in the $z \sim 10$ LBG sample used here.

The relatively high galaxy bias we measure, even if corrected for the impact of non-linear scales (see Section 4.2) provides an additional argument for a high purity of the LBG sample from W25. Uncertainties in photometric redshifts artificially weaken the clustering signal, since interloper populations are randomly distributed relative to the target population. The effect of including unassociated galaxies would dilute the measured clustering by a factor of $(1 + f_{\text{interlopers}})^2$ (see, e.g. Williams et al. 2011). Conversely formulated, if our sample is subject to substantial contamination, this

would only strengthen our tentative finding of a high cosmic variance and strong galaxy clustering at $z \sim 10$.

4.6. Combined Implications of UVLF and Clustering Measurements

The findings of W25 suggest a rapid build-up of galaxies at cosmic dawn with ρ_{UV} increasing by a factor $\gtrsim 50$ from $z \sim 17$ to $z \sim 10$. We now add the constraint that at $z \sim 10$, UV-bright galaxies are highly clustered. Below, we further discuss the implications of combining these two findings in the context of theoretical models.

We first use the modeling framework from Shuntov et al. (2025) that was already used in W25 to explore models that can reproduce the UVLF by either enhancing the SFE and/or σ_{UV} . As shown there, a model with a slightly enhanced SFE, characterized by $\epsilon_0 = 0.3$, where ϵ_0 is the normalization of the *instantaneous* SFE ($\epsilon = \dot{M}_*/(f_b \dot{M}_{\text{halo}})$), and $\sigma_{\text{UV}} = 0.6$ matches the UVLF at $z \sim 10$. Here, we measure the linear galaxy bias from this model for galaxies with $M_{\text{UV}} < -20$, and using Equation (14) in Shuntov et al. (2025), and find a bias value of 12.7, close to our measured and converted value of $14.4^{+5.7}_{-4.8}$ (see Section 4.2). We also tested that enhancing σ_{UV} or ϵ_0 further increases the galaxy abundance and decreases the bias, albeit to varying degrees, consistent with previous findings. In the Shuntov et al. (2025) modeling framework, the combined measurements of the UVLF in W25 and the clustering in this work are con-

sistent with a model with a somewhat enhanced SFE, and a mild contribution of star formation stochasticity.

While our measurements are not constraining enough to confidently rule out any model, they tentatively disfavor models where UV-scatter is the dominant driver of the high abundance of UV-bright galaxies at $z \sim 10$. In this context, [Carvajal-Bohorquez et al. \(2025\)](#) recently analyzed a photometric sample of galaxies at $6 < z < 12$ from JADES, and measured maximum values of $\sigma_{\text{UV}} = 0.72 \pm 0.02$ mag and $\text{SFE} = 0.06 \pm 0.01$, concluding that neither of them is solely responsible for the high UVLF at $z > 10$, consistent with our findings. Similarly [Simmonds et al. \(2025\)](#) compiled photometric data from JADES to characterize the star-forming main sequence and its scatter across cosmic time. They measured $\sigma_{\text{UV}} = 0.6 - 0.75$ at $6 < z \leq 9$, again suggesting that UV-scatter alone is unlikely to drive the observed abundance of UV-bright galaxies at $z \gtrsim 9$.

Proposed physical models for the high abundance of UV bright galaxies at $z \sim 10$ that do not rely on burstiness include the DMSFE ([Somerville et al. 2025](#)), which we discussed above and which provides the best fit to our measurements within our simple modeling framework. Other proposed models include the feedback-free starburst scenario ([Dekel et al. 2023](#)) which implies high SFEs in the most massive halos, a lack of dust attenuation ([Ferrara et al. 2023](#)), and a more top-heavy IMF in highly star-forming regions ([Hutter et al. 2025](#); see also [Mauerhofer et al. 2025](#)). A more in-depth analysis of the combined implications of these models for the UVLF and the clustering strength of galaxies at $z \sim 10$ is beyond the scope of this work. [W25](#) further mentioned the model proposed by [Donnan et al. \(2025\)](#) who pointed out that the abundance of UV-bright galaxies at $z \gtrsim 10$ may be attributed to the ever younger ages of stellar populations at high redshift, decreasing their mass-to-light ratio. Taken at face value, their model suggests a typical formation redshift of galaxies of $z \sim 15$ which would then imply a rapid drop in the number density of galaxies at those redshifts, consistent with the results of [W25](#). We note here that a decrease in the mass-to-light ratio is reflected in our model implementing a global boost in the UV-luminosity (top row of panels in Figure 2). This scenario is therefore consistent with our cosmic variance measurements, and is perhaps best tested through targeted searches for $z \gtrsim 15$ galaxies.

4.7. Cosmology, Assembly and Environmental Biases

All of the models tested here are based on relations with one halo feature only: halo mass. However, galaxy properties and their clustering are known to be strongly associated with both internal properties beyond halo

mass (e.g. age and concentration), and their exact *assembly* and *environments*, especially on small scales ([Hearin et al. 2016](#); [Zentner et al. 2019](#); [Jespersen et al. 2022](#); [Chuang et al. 2024](#); [Wu et al. 2024](#); [Lim et al. 2025](#)). In fact, environmental bias has been shown to be the likely origin of some extreme outlier galaxies observed with JWST ([Jespersen et al. 2025a](#)). Future work should consider whether clustering amplitudes of model galaxies could be raised by e.g. preferentially populating older halos as suggested by [Hearin et al. \(2016\)](#), while still raising the number density to the necessary levels. However, these differences can only truly be probed with constraints that include the next generation of pure-parallel imaging surveys (see Figures 6 and 7).

It is furthermore worth noting that all models tested here assume a fixed set of cosmological parameters, which artificially shrinks the model uncertainties. Since we do not have access to **UniverseMachine** simulations with varying cosmology, we can instead estimate the impact by calculating the changes in the matter field variance while varying the fiducial WMAP cosmological parameters under 1σ uncertainties from [Planck Collaboration et al. \(2020\)](#). Assuming no covariance between parameters, the resulting uncertainty on σ_{DM} is on the order of 6%, which is subdominant to our measurement uncertainties and inter-model differences. However, this also ignores any possible feedback between cosmology and galaxy formation models.

5. SUMMARY AND CONCLUSIONS

In this work, we use the sample of LBGs at $z \sim 10$ compiled by [W25](#) from a combination of legacy and pure parallel imaging from PANORAMIC to perform a measurement of their cosmic variance σ_{CV} . We follow two complementary approaches to measure σ_{CV} : bootstrapping the number count per field and its variance (Equation 4), and MCMC forward modeling of the distribution of number counts per field. This yields high values suggesting cosmic variance driven uncertainties in the galaxy number count per NIRCam pointing of 100 – 200% for galaxies with $M_{\text{UV}} < -19.5$, consistent with values measured from the **UniverseMachine** using the same methods. Converting these measurements to a galaxy bias following [Robertson \(2010\)](#) yields values ranging from $b_{g,\text{CV}} \sim 30 - 50$ for different M_{UV} limits. Such high bias values can be understood in the context of clustering on small, non-linear scales contributing to the observed field-to-field variance. Quantifying this effect using the **UniverseMachine**, we show that for NIRCam pointing sized fields, the galaxy bias inferred from the cosmic variance is a factor of 3 – 5 higher than the linear bias for different M_{UV} limits.

Different models proposed to explain the high observed abundance of UV-bright galaxies at $z \gtrsim 10$ differ in terms of their predictions for the clustering strength of galaxies. A direct measurement of σ_{UV} at $z \sim 10$ can therefore break degeneracies between models. We explore this by implementing simple models in the `UniverseMachine` mimicking different physical processes proposed in the literature, and compare their combined predictions for the abundance and the cosmic variance of galaxies at $z \sim 10$ to our measurements. Our simple models can be categorized in three classes: (1) models that boost the UV-luminosity of galaxies by ΔM_{UV} , (2) models that enhance the SFE, and (3) models that increase the scatter in the $M_{\text{UV}}-M_h$ relation (σ_{UV}). We implement two versions of each model class: (1) a global boost by ΔM_{UV} for all galaxies, and a boost only above a certain threshold in halo mass, (2) a global constant SFE across all galaxies, and a power-law scaling of the SFE with halo mass, and (3) a global constant σ_{UV} , and a scaling of σ_{UV} with halo mass (more scatter in lower mass halos, following [Sun et al. 2023](#)).

All these models can increase the abundance of $z \sim 10$ galaxies to match our observational constraints, but simultaneously weaken the clustering signal (decrease σ_{UV}) by placing galaxies at fixed M_{UV} in lower mass halos that are more abundant, and less clustered. Nevertheless, models differ in their combined predictions for the UVLF and the clustering. Quantifying the tension between models and the data across distinct M_{UV} bins (i.e. along the UVLF), we find that a global increase in the SFE, as well as models that increase σ_{UV} are disfavored at $\gtrsim 2\sigma$ significance, relative to the best-fitting model that implements a scaling of the SFE with halo mass as $\text{SFE} \propto M_{\text{halo}}^{0.5}$, akin to the DMSFE proposed by [Somerville et al. \(2025\)](#). With only 50 additional lines of sight, that could easily be obtained in a single dedicated pure parallel imaging survey, these model differences could be increased to $> 3\sigma$.

Wider area deep NIRCam imaging along a larger number of independent lines of sight is required to obtain a more robust measurement of cosmic variance at $z \sim 10$, and possibly beyond. Such data can be most efficiently acquired in the pure parallel imaging mode and yield invaluable constraints on the clustering of galaxies at cosmic dawn. They can help discriminate between different models invoked to explain the abundance of UV-bright galaxies so early in the Universe, and shed light on the physical processes driving galaxy growth in the first few hundred Myr after the Big Bang.

ACKNOWLEDGEMENTS

We thank Oliver Hahn and Jens Stücker for the productive and informative discussion of the effect of clustering on non-linear scales on our cosmic variance measurements. This work is based on observations made with the NASA/ESA/CSA James Webb Space Telescope. The data were obtained from the Mikulski Archive for Space Telescopes at the Space Telescope Science Institute, which is operated by the Association of Universities for Research in Astronomy, Inc., under NASA contract NAS 5-03127 for JWST. These observations are associated with program #2514. Support for program #2514 was provided by NASA through a grant from the Space Telescope Science Institute, which is operated by the Association of Universities for Research in Astronomy, Inc., under NASA contract NAS 5-03127. The Cosmic Dawn Center is funded by the Danish National Research Foundation (DNRF140). This work has received funding from the Swiss State Secretariat for Education, Research and Innovation (SERI) under contract number MB22.00072, as well as from the Swiss National Science Foundation (SNSF) through project grant 200020_207349. The work of C.C.W. is supported by NOIRLab, which is managed by the Association of Universities for Research in Astronomy (AURA) under a cooperative agreement with the National Science Foundation. P. Dayal warmly acknowledges support from an NSERC discovery grant (RGPIN-2025-06182).

Facilities: JWST(NIRSpec, NIRCam)

REFERENCES

Adams, N. J., Conselice, C. J., Ferreira, L., et al. 2023, MNRAS, 518, 4755, doi: [10.1093/mnras/stac3347](https://doi.org/10.1093/mnras/stac3347)

Adams, N. J., Conselice, C. J., Austin, D., et al. 2024, ApJ, 965, 169, doi: [10.3847/1538-4357/ad2a7b](https://doi.org/10.3847/1538-4357/ad2a7b)

Arrabal Haro, P., Dickinson, M., Finkelstein, S. L., et al. 2023, Nature, 622, 707, doi: [10.1038/s41586-023-06521-7](https://doi.org/10.1038/s41586-023-06521-7)

Asada, Y., Willott, C., Muzzin, A., et al. 2025, arXiv e-prints, arXiv:2507.03124. <https://arxiv.org/abs/2507.03124>

Atek, H., Chemerynska, I., Wang, B., et al. 2023, MNRAS, 524, 5486, doi: [10.1093/mnras/stad1998](https://doi.org/10.1093/mnras/stad1998)

Barone-Nugent, R. L., Trenti, M., Wyithe, J. S. B., et al. 2014, ApJ, 793, 17, doi: [10.1088/0004-637X/793/1/17](https://doi.org/10.1088/0004-637X/793/1/17)

Behroozi, P., Wechsler, R. H., Hearin, A. P., & Conroy, C. 2019, MNRAS, 488, 3143, doi: [10.1093/mnras/stz1182](https://doi.org/10.1093/mnras/stz1182)

Berlind, A. A., & Weinberg, D. H. 2002, ApJ, 575, 587, doi: [10.1086/341469](https://doi.org/10.1086/341469)

Bertin, E., & Arnouts, S. 1996, A&AS, 117, 393, doi: [10.1051/aas:1996164](https://doi.org/10.1051/aas:1996164)

Blanc, G. A., Lira, P., Barrientos, L. F., et al. 2008, ApJ, 681, 1099, doi: [10.1086/588018](https://doi.org/10.1086/588018)

Bouwens, R. J., Oesch, P. A., Labb  , I., et al. 2016, ApJ, 830, 67, doi: [10.3847/0004-637X/830/2/67](https://doi.org/10.3847/0004-637X/830/2/67)

Boylan-Kolchin, M. 2024, arXiv e-prints, arXiv:2407.10900, doi: [10.48550/arXiv.2407.10900](https://doi.org/10.48550/arXiv.2407.10900)

Brammer, G. 2023, grizli, 1.9.11, Zenodo, Zenodo, doi: [10.5281/zenodo.8370018](https://doi.org/10.5281/zenodo.8370018)

Brammer, G. B., van Dokkum, P. G., & Coppi, P. 2008, The Astrophysical Journal, 686, 1503

Budav  i, T., Connolly, A. J., Szalay, A. S., et al. 2003, ApJ, 595, 59, doi: [10.1086/377168](https://doi.org/10.1086/377168)

Cameron, A. J., Trenti, M., Livermore, R. C., & van der Velden, C. 2019, MNRAS, 483, 1922, doi: [10.1093/mnras/sty3069](https://doi.org/10.1093/mnras/sty3069)

Carnall, A. C., McLure, R. J., Dunlop, J. S., & Dav  , R. 2018, MNRAS, 480, 4379, doi: [10.1093/mnras/sty2169](https://doi.org/10.1093/mnras/sty2169)

Carniani, S., Hainline, K., D'Eugenio, F., et al. 2024, Nature, 633, 318, doi: [10.1038/s41586-024-07860-9](https://doi.org/10.1038/s41586-024-07860-9)

Carrasco, D., Trenti, M., Mutch, S., & Oesch, P. A. 2018, PASA, 35, e022, doi: [10.1017/pasa.2018.17](https://doi.org/10.1017/pasa.2018.17)

Carvajal-Bohorquez, C., Ciesla, L., Laporte, N., et al. 2025, arXiv e-prints, arXiv:2507.13160, doi: [10.48550/arXiv.2507.13160](https://doi.org/10.48550/arXiv.2507.13160)

Casey, C. M., Kartaltepe, J. S., Drakos, N. E., et al. 2023, ApJ, 954, 31, doi: [10.3847/1538-4357/acc2bc](https://doi.org/10.3847/1538-4357/acc2bc)

Casey, C. M., Akins, H. B., Shuntov, M., et al. 2024, ApJ, 965, 98, doi: [10.3847/1538-4357/ad2075](https://doi.org/10.3847/1538-4357/ad2075)

Castellano, M., Fontana, A., Treu, T., et al. 2022, ApJL, 938, L15, doi: [10.3847/2041-8213/ac94d0](https://doi.org/10.3847/2041-8213/ac94d0)

Castellano, M., Napolitano, L., Fontana, A., et al. 2024, ApJ, 972, 143, doi: [10.3847/1538-4357/ad5f88](https://doi.org/10.3847/1538-4357/ad5f88)

Chuang, C.-Y., Jespersen, C. K., Lin, Y.-T., Ho, S., & Genel, S. 2024, ApJ, 965, 101, doi: [10.3847/1538-4357/ad2b6c](https://doi.org/10.3847/1538-4357/ad2b6c)

Cooray, A., & Sheth, R. 2002, PhR, 372, 1, doi: [10.1016/S0370-1573\(02\)00276-4](https://doi.org/10.1016/S0370-1573(02)00276-4)

Cueto, E. R., Hutter, A., Dayal, P., et al. 2024, A&A, 686, A138, doi: [10.1051/0004-6361/202349017](https://doi.org/10.1051/0004-6361/202349017)

Curtis-Lake, E., Carniani, S., Cameron, A., et al. 2023, Nature Astronomy, 7, 622, doi: [10.1038/s41550-023-01918-w](https://doi.org/10.1038/s41550-023-01918-w)

Dalmasso, N., Leethochawalit, N., Trenti, M., & Boyett, K. 2024, MNRAS, 533, 2391, doi: [10.1093/mnras/stae2006](https://doi.org/10.1093/mnras/stae2006)

Dayal, P., Ferrara, A., Dunlop, J. S., & Pacucci, F. 2014, MNRAS, 445, 2545, doi: [10.1093/mnras/stu1848](https://doi.org/10.1093/mnras/stu1848)

Dekel, A., Sarkar, K. C., Birnboim, Y., Mandelker, N., & Li, Z. 2023, MNRAS, 523, 3201, doi: [10.1093/mnras/stad1557](https://doi.org/10.1093/mnras/stad1557)

Donnan, C. T., Dunlop, J. S., McLure, R. J., McLeod, D. J., & Cullen, F. 2025, arXiv e-prints, arXiv:2501.03217, doi: [10.48550/arXiv.2501.03217](https://doi.org/10.48550/arXiv.2501.03217)

Donnan, C. T., McLeod, D. J., Dunlop, J. S., et al. 2023, MNRAS, 518, 6011, doi: [10.1093/mnras/stac3472](https://doi.org/10.1093/mnras/stac3472)

Donnan, C. T., McLure, R. J., Dunlop, J. S., et al. 2024, MNRAS, 533, 3222, doi: [10.1093/mnras/stae2037](https://doi.org/10.1093/mnras/stae2037)

Feldmann, R., Boylan-Kolchin, M., Bullock, J. S., et al. 2025, MNRAS, 536, 988, doi: [10.1093/mnras/stae2633](https://doi.org/10.1093/mnras/stae2633)

Ferrara, A., Pallottini, A., & Dayal, P. 2023, MNRAS, 522, 3986, doi: [10.1093/mnras/stad1095](https://doi.org/10.1093/mnras/stad1095)

Finkelstein, S. L., Bagley, M. B., Ferguson, H. C., et al. 2023, ApJL, 946, L13, doi: [10.3847/2041-8213/acade4](https://doi.org/10.3847/2041-8213/acade4)

Finkelstein, S. L., Leung, G. C. K., Bagley, M. B., et al. 2024, ApJL, 969, L2, doi: [10.3847/2041-8213/ad4495](https://doi.org/10.3847/2041-8213/ad4495)

Foreman-Mackey, D., Hogg, D. W., Lang, D., & Goodman, J. 2013, PASP, 125, 306, doi: [10.1086/670067](https://doi.org/10.1086/670067)

Fujimoto, S., Wang, B., Weaver, J. R., et al. 2024, ApJ, 977, 250, doi: [10.3847/1538-4357/ad9027](https://doi.org/10.3847/1538-4357/ad9027)

Gelli, V., Mason, C., & Hayward, C. C. 2024, ApJ, 975, 192, doi: [10.3847/1538-4357/ad7b36](https://doi.org/10.3847/1538-4357/ad7b36)

Grogan, N. A., Kocevski, D. D., Faber, S. M., et al. 2011, ApJS, 197, 35, doi: [10.1088/0067-0049/197/2/35](https://doi.org/10.1088/0067-0049/197/2/35)

Hainline, K. N., Johnson, B. D., Robertson, B., et al. 2024, ApJ, 964, 71, doi: [10.3847/1538-4357/ad1ee4](https://doi.org/10.3847/1538-4357/ad1ee4)

Harikane, Y., Nakajima, K., Ouchi, M., et al. 2024, ApJ, 960, 56, doi: [10.3847/1538-4357/ad0b7e](https://doi.org/10.3847/1538-4357/ad0b7e)

Harikane, Y., Ouchi, M., Ono, Y., et al. 2016, ApJ, 821, 123, doi: [10.3847/0004-637X/821/2/123](https://doi.org/10.3847/0004-637X/821/2/123)

—. 2018, PASJ, 70, S11, doi: [10.1093/pasj/pss097](https://doi.org/10.1093/pasj/pss097)

Harikane, Y., Ouchi, M., Oguri, M., et al. 2023, *ApJS*, 265, 5, doi: [10.3847/1538-4365/acaaa9](https://doi.org/10.3847/1538-4365/acaaa9)

Hearin, A. P., Zentner, A. R., van den Bosch, F. C., Campbell, D., & Tollerud, E. 2016, *MNRAS*, 460, 2552, doi: [10.1093/mnras/stw840](https://doi.org/10.1093/mnras/stw840)

Hegde, S., Wyatt, M. M., & Furlanetto, S. R. 2024, *JCAP*, 2024, 025, doi: [10.1088/1475-7516/2024/08/025](https://doi.org/10.1088/1475-7516/2024/08/025)

Hildebrandt, H., Pielorz, J., Erben, T., et al. 2009, *A&A*, 498, 725, doi: [10.1051/0004-6361/200811042](https://doi.org/10.1051/0004-6361/200811042)

Hinshaw, G., Larson, D., Komatsu, E., et al. 2013, *ApJS*, 208, 19, doi: [10.1088/0067-0049/208/2/19](https://doi.org/10.1088/0067-0049/208/2/19)

Hogg, D. W., Bovy, J., & Lang, D. 2010, arXiv e-prints, arXiv:1008.4686, doi: [10.48550/arXiv.1008.4686](https://doi.org/10.48550/arXiv.1008.4686)

Hutter, A., Cueto, E. R., Dayal, P., et al. 2025, *A&A*, 694, A254, doi: [10.1051/0004-6361/202452460](https://doi.org/10.1051/0004-6361/202452460)

Ishigaki, M., Kawamata, R., Ouchi, M., et al. 2018, *ApJ*, 854, 73, doi: [10.3847/1538-4357/aaa544](https://doi.org/10.3847/1538-4357/aaa544)

Ishikawa, S., Kashikawa, N., Toshikawa, J., et al. 2017, *ApJ*, 841, 8, doi: [10.3847/1538-4357/aa6d64](https://doi.org/10.3847/1538-4357/aa6d64)

Jeffreys, H. 1946, *Proceedings of the Royal Society of London. Series A. Mathematical and Physical Sciences*, 186, 453

Jespersen, C. K., Carnall, A. C., & Lovell, C. C. 2025a, *ApJL*, 988, L19, doi: [10.3847/2041-8213/adeb7c](https://doi.org/10.3847/2041-8213/adeb7c)

Jespersen, C. K., Cranmer, M., Melchior, P., et al. 2022, *ApJ*, 941, 7, doi: [10.3847/1538-4357/ac9b18](https://doi.org/10.3847/1538-4357/ac9b18)

Jespersen, C. K., Melchior, P., Spergel, D. N., et al. 2025b, arXiv e-prints, arXiv:2503.03816, doi: [10.48550/arXiv.2503.03816](https://doi.org/10.48550/arXiv.2503.03816)

Jespersen, C. K., Steinhardt, C. L., Somerville, R. S., & Lovell, C. C. 2025c, *ApJ*, 982, 23, doi: [10.3847/1538-4357/adb422](https://doi.org/10.3847/1538-4357/adb422)

Jose, C., Baugh, C. M., Lacey, C. G., & Subramanian, K. 2017, *MNRAS*, 469, 4428, doi: [10.1093/mnras/stx1014](https://doi.org/10.1093/mnras/stx1014)

Jose, C., Lacey, C. G., & Baugh, C. M. 2016, *MNRAS*, 463, 270, doi: [10.1093/mnras/stw1702](https://doi.org/10.1093/mnras/stw1702)

Klypin, A., Yepes, G., Gottlöber, S., Prada, F., & Heß, S. 2016, *MNRAS*, 457, 4340, doi: [10.1093/mnras/stw248](https://doi.org/10.1093/mnras/stw248)

Kravtsov, A., & Belokurov, V. 2024, arXiv e-prints, arXiv:2405.04578, doi: [10.48550/arXiv.2405.04578](https://doi.org/10.48550/arXiv.2405.04578)

Leethochawalit, N., Trenti, M., Morishita, T., Roberts-Borsani, G., & Treu, T. 2022, *MNRAS*, 509, 5836, doi: [10.1093/mnras/stab3265](https://doi.org/10.1093/mnras/stab3265)

Li, C., Kauffmann, G., Jing, Y. P., et al. 2006, *MNRAS*, 368, 21, doi: [10.1111/j.1365-2966.2006.10066.x](https://doi.org/10.1111/j.1365-2966.2006.10066.x)

Li, Z., Dekel, A., Sarkar, K. C., et al. 2024, *A&A*, 690, A108, doi: [10.1051/0004-6361/202348727](https://doi.org/10.1051/0004-6361/202348727)

Lim, S., Tacchella, S., Maiolino, R., Lovell, C. C., & Schaye, J. 2025, arXiv e-prints, arXiv:2511.09618, doi: [10.48550/arXiv.2511.09618](https://doi.org/10.48550/arXiv.2511.09618)

Lin, L., Dickinson, M., Jian, H.-Y., et al. 2012, *ApJ*, 756, 71, doi: [10.1088/0004-637X/756/1/71](https://doi.org/10.1088/0004-637X/756/1/71)

López-Sanjuan, C., Cenarro, A. J., Hernández-Monteagudo, C., et al. 2015, *A&A*, 582, A16, doi: [10.1051/0004-6361/201526731](https://doi.org/10.1051/0004-6361/201526731)

Lu, S., Frenk, C. S., Bose, S., et al. 2025, *MNRAS*, 536, 1018, doi: [10.1093/mnras/stae2646](https://doi.org/10.1093/mnras/stae2646)

Mason, C. A., Trenti, M., & Treu, T. 2015, *ApJ*, 813, 21, doi: [10.1088/0004-637X/813/1/21](https://doi.org/10.1088/0004-637X/813/1/21)

—. 2023, *MNRAS*, 521, 497, doi: [10.1093/mnras/stad035](https://doi.org/10.1093/mnras/stad035)

Mauerhofer, V., Dayal, P., Haehnelt, M. G., et al. 2025, *A&A*, 696, A157, doi: [10.1051/0004-6361/202554042](https://doi.org/10.1051/0004-6361/202554042)

McCracken, H. J., Wolk, M., Colombi, S., et al. 2015, *MNRAS*, 449, 901, doi: [10.1093/mnras/stv305](https://doi.org/10.1093/mnras/stv305)

Meneux, B., Guzzo, L., de la Torre, S., et al. 2009, *A&A*, 505, 463, doi: [10.1051/0004-6361/200912314](https://doi.org/10.1051/0004-6361/200912314)

Mirocha, J. 2020, *MNRAS*, 499, 4534, doi: [10.1093/mnras/staa3150](https://doi.org/10.1093/mnras/staa3150)

Mo, H. J., & White, S. D. M. 1996, *MNRAS*, 282, 347, doi: [10.1093/mnras/282.2.347](https://doi.org/10.1093/mnras/282.2.347)

Morishita, T., Mason, C. A., Kreilgaard, K. C., et al. 2025, *ApJ*, 983, 152, doi: [10.3847/1538-4357/adbbdc](https://doi.org/10.3847/1538-4357/adbbdc)

Moster, B. P., Somerville, R. S., Newman, J. A., & Rix, H.-W. 2011, *ApJ*, 731, 113, doi: [10.1088/0004-637X/731/2/113](https://doi.org/10.1088/0004-637X/731/2/113)

Muñoz, J. B., Mirocha, J., Furlanetto, S., & Sabti, N. 2023, *MNRAS*, 526, L47, doi: [10.1093/mnrasl/slad115](https://doi.org/10.1093/mnrasl/slad115)

Naidu, R. P., Oesch, P. A., van Dokkum, P., et al. 2022, *ApJL*, 940, L14, doi: [10.3847/2041-8213/ac9b22](https://doi.org/10.3847/2041-8213/ac9b22)

Naidu, R. P., Oesch, P. A., Brammer, G., et al. 2025, arXiv e-prints, arXiv:2505.11263, <https://arxiv.org/abs/2505.11263>

Newman, J. A., & Davis, M. 2002, *ApJ*, 564, 567, doi: [10.1086/324148](https://doi.org/10.1086/324148)

Newman, J. A., & Moster, B. P. 2014, *QUICKCV: Cosmic variance calculator*, Astrophysics Source Code Library, record ascl:1402.012

Norberg, P., Baugh, C. M., Hawkins, E., et al. 2002, *MNRAS*, 332, 827, doi: [10.1046/j.1365-8711.2002.05348.x](https://doi.org/10.1046/j.1365-8711.2002.05348.x)

Oesch, P. A., Bouwens, R. J., Illingworth, G. D., Labbé, I., & Stefanon, M. 2018, *ApJ*, 855, 105, doi: [10.3847/1538-4357/aab03f](https://doi.org/10.3847/1538-4357/aab03f)

Oke, J. B., & Gunn, J. E. 1983, *ApJ*, 266, 713, doi: [10.1086/160817](https://doi.org/10.1086/160817)

Pacucci, F., Dayal, P., Harikane, Y., Inoue, A. K., & Loeb, A. 2022, *MNRAS*, 514, L6, doi: [10.1093/mnrasl/slac035](https://doi.org/10.1093/mnrasl/slac035)

Paquereau, L., Laigle, C., McCracken, H. J., et al. 2025, arXiv e-prints, arXiv:2501.11674, doi: [10.48550/arXiv.2501.11674](https://doi.org/10.48550/arXiv.2501.11674)

Pérez-González, P. G., Costantin, L., Langeroodi, D., et al. 2023, ApJL, 951, L1, doi: [10.3847/2041-8213/acd9d0](https://doi.org/10.3847/2041-8213/acd9d0)

Planck Collaboration, Aghanim, N., Akrami, Y., et al. 2020, A&A, 641, A6, doi: [10.1051/0004-6361/201833910](https://doi.org/10.1051/0004-6361/201833910)

Robertson, B., Johnson, B. D., Tacchella, S., et al. 2024, ApJ, 970, 31, doi: [10.3847/1538-4357/ad463d](https://doi.org/10.3847/1538-4357/ad463d)

Robertson, B. E. 2010, ApJL, 716, L229, doi: [10.1088/2041-8205/716/2/L229](https://doi.org/10.1088/2041-8205/716/2/L229)

Rodríguez-Puebla, A., Behroozi, P., Primack, J., et al. 2016, MNRAS, 462, 893, doi: [10.1093/mnras/stw1705](https://doi.org/10.1093/mnras/stw1705)

Shen, X., Vogelsberger, M., Boylan-Kolchin, M., Tacchella, S., & Kannan, R. 2023, MNRAS, 525, 3254, doi: [10.1093/mnras/stad2508](https://doi.org/10.1093/mnras/stad2508)

Shen, X., Vogelsberger, M., Boylan-Kolchin, M., Tacchella, S., & Naidu, R. P. 2024, MNRAS, 533, 3923, doi: [10.1093/mnras/stae1932](https://doi.org/10.1093/mnras/stae1932)

Shuntov, M., Oesch, P. A., Toft, S., et al. 2025, arXiv e-prints, arXiv:2503.14280, doi: [10.48550/arXiv.2503.14280](https://doi.org/10.48550/arXiv.2503.14280)

Simmonds, C., Tacchella, S., McClymont, W., et al. 2025, arXiv e-prints, arXiv:2508.04410, doi: [10.48550/arXiv.2508.04410](https://doi.org/10.48550/arXiv.2508.04410)

Skelton, R. E., Whitaker, K. E., Momcheva, I. G., et al. 2014, ApJS, 214, 24, doi: [10.1088/0067-0049/214/2/24](https://doi.org/10.1088/0067-0049/214/2/24)

Somerville, R. S., Lee, K., Ferguson, H. C., et al. 2004, ApJL, 600, L171, doi: [10.1086/378628](https://doi.org/10.1086/378628)

Somerville, R. S., Yung, L. Y. A., Lancaster, L., et al. 2025, arXiv e-prints, arXiv:2505.05442, doi: [10.48550/arXiv.2505.05442](https://doi.org/10.48550/arXiv.2505.05442)

Song, M., Finkelstein, S. L., Ashby, M. L. N., et al. 2016, ApJ, 825, 5, doi: [10.3847/0004-637X/825/1/5](https://doi.org/10.3847/0004-637X/825/1/5)

Springel, V., White, S. D. M., Jenkins, A., et al. 2005, Nature, 435, 629, doi: [10.1038/nature03597](https://doi.org/10.1038/nature03597)

Steinhardt, C. L., Jespersen, C. K., & Linzer, N. B. 2021, ApJ, 923, 8, doi: [10.3847/1538-4357/ac2a2f](https://doi.org/10.3847/1538-4357/ac2a2f)

Sun, G., Faucher-Giguère, C.-A., Hayward, C. C., et al. 2023, ApJL, 955, L35, doi: [10.3847/2041-8213/acf85a](https://doi.org/10.3847/2041-8213/acf85a)

Tacchella, S., Bose, S., Conroy, C., Eisenstein, D. J., & Johnson, B. D. 2018, ApJ, 868, 92, doi: [10.3847/1538-4357/aae8e0](https://doi.org/10.3847/1538-4357/aae8e0)

Tinker, J. L., Robertson, B. E., Kravtsov, A. V., et al. 2010, ApJ, 724, 878, doi: [10.1088/0004-637X/724/2/878](https://doi.org/10.1088/0004-637X/724/2/878)

Trinca, A., Schneider, R., Valiante, R., et al. 2024, MNRAS, 529, 3563, doi: [10.1093/mnras/stae651](https://doi.org/10.1093/mnras/stae651)

Valentino, F., Brammer, G., Gould, K. M. L., et al. 2023, ApJ, 947, 20, doi: [10.3847/1538-4357/acbefa](https://doi.org/10.3847/1538-4357/acbefa)

Wake, D. A., Whitaker, K. E., Labb  , I., et al. 2011, ApJ, 728, 46, doi: [10.1088/0004-637X/728/1/46](https://doi.org/10.1088/0004-637X/728/1/46)

Weaver, J. R., Cutler, S. E., Pan, R., et al. 2024, ApJS, 270, 7, doi: [10.3847/1538-4365/ad07e0](https://doi.org/10.3847/1538-4365/ad07e0)

Weibel, A., Oesch, P. A., Barrufet, L., et al. 2024, MNRAS, 533, 1808, doi: [10.1093/mnras/stae1891](https://doi.org/10.1093/mnras/stae1891)

Weibel, A., Oesch, P. A., Williams, C. C., et al. 2025, arXiv e-prints, arXiv:2507.06292, <https://arxiv.org/abs/2507.06292>

Whitaker, K. E., Ashas, M., Illingworth, G., et al. 2019, ApJS, 244, 16, doi: [10.3847/1538-4365/ab3853](https://doi.org/10.3847/1538-4365/ab3853)

Whitler, L., Stark, D. P., Topping, M. W., et al. 2025, arXiv e-prints, arXiv:2501.00984, doi: [10.48550/arXiv.2501.00984](https://doi.org/10.48550/arXiv.2501.00984)

Williams, C. C., Giavalisco, M., Porciani, C., et al. 2011, ApJ, 733, 92, doi: [10.1088/0004-637X/733/2/92](https://doi.org/10.1088/0004-637X/733/2/92)

Williams, C. C., Curtis-Lake, E., Hainline, K. N., et al. 2018, ApJS, 236, 33, doi: [10.3847/1538-4365/aabcbb](https://doi.org/10.3847/1538-4365/aabcbb)

Williams, C. C., Oesch, P. A., Weibel, A., et al. 2025, ApJ, 979, 140, doi: [10.3847/1538-4357/ad97bc](https://doi.org/10.3847/1538-4357/ad97bc)

Willott, C. J., Desprez, G., Asada, Y., et al. 2024, ApJ, 966, 74, doi: [10.3847/1538-4357/ad35bc](https://doi.org/10.3847/1538-4357/ad35bc)

Wu, J. F., Jespersen, C. K., & Wechsler, R. H. 2024, ApJ, 976, 37, doi: [10.3847/1538-4357/ad7bb3](https://doi.org/10.3847/1538-4357/ad7bb3)

Ye, I., Bull, P., Bowler, R. A. A., et al. 2025, MNRAS, 543, 3196, doi: [10.1093/mnras/staf1651](https://doi.org/10.1093/mnras/staf1651)

Yung, L. Y. A., Somerville, R. S., Finkelstein, S. L., Wilkins, S. M., & Gardner, J. P. 2024, MNRAS, 527, 5929, doi: [10.1093/mnras/stad3484](https://doi.org/10.1093/mnras/stad3484)

Zehavi, I., Zheng, Z., Weinberg, D. H., et al. 2005, ApJ, 630, 1, doi: [10.1086/431891](https://doi.org/10.1086/431891)

Zentner, A. R., Hearin, A., van den Bosch, F. C., Lange, J. U., & Villarreal, A. S. 2019, MNRAS, 485, 1196, doi: [10.1093/mnras/stz470](https://doi.org/10.1093/mnras/stz470)

APPENDIX

A. POSTERIOR DISTRIBUTIONS OF THE COSMIC VARIANCE FITS

Figure 8 shows the posterior distributions of the MCMC-fits to the completeness corrected number counts of galaxies along 34 independent lines of sight, and for three different M_{UV} limits, as explained in Section 2.4.2. The widths of these distributions could potentially be underestimated due to the lack of inclusion of the uncertainty in the completeness correction. The nominal uncertainty in the completeness is small, but also likely to be underestimated (Carnall et al. 2018; Jespersen et al. 2025b).

B. BEST-FITTING PARAMETERS OF TESTED MODELS

Below, we list the constraints we get on the model parameters for the different tested models. Note that the quoted uncertainties are calculated by considering the typical 0.5 value increase in the log-likelihood on either side, which *does not* take into account any model misspecification corrections for a model that does not actually provide a good fit. As discussed in Jespersen et al. (2025b), this results in the quoted uncertainties being underestimated, and the central values being biased. The more misspecified the model, the more severe the issue, which is why we have focused on the task of determining *which* model is most appropriate, rather than constraining the parameters that characterize a specific model.

Model Name	Parameter	Best-fit value
Global ΔM_{UV} (A1)	ΔM_{UV}	$1.02^{+0.08}_{-0.07}$
$\Delta M_{\text{UV}}: M_{\text{halo}} \geq 10^{10} M_{\odot}$ (A2)	ΔM_{UV}	$1.01^{+0.08}_{-0.08}$
$\Delta M_{\text{UV}}: M_{\text{halo}} \geq 10^{10.5} M_{\odot}$ (A2)	ΔM_{UV}	$0.93^{+0.13}_{-0.19}$
Global SFE (B1)	SFE	$0.098^{+0.004}_{-0.006}$
DMSFE: $\text{SFE} \propto M_{\text{halo}}^{0.5}$ (B2)	SFE_{peak}	$0.63^{+0.03}_{-0.02}$
DMSFE: $\text{SFE} \propto M_{\text{halo}}^{0.6}$ (B2)	SFE_{peak}	$0.94^{+0.06}_{-0.06}$
Global σ_{UV} (C1)	σ_{UV}	$1.21^{+0.04}_{-0.04}$
M_{halo} -dependent σ_{UV} (C2)	$\sigma_{\text{UV, norm}}$	$1.11^{+0.06}_{-0.05}$

Table 1. The best-fitting parameters for all tested models.

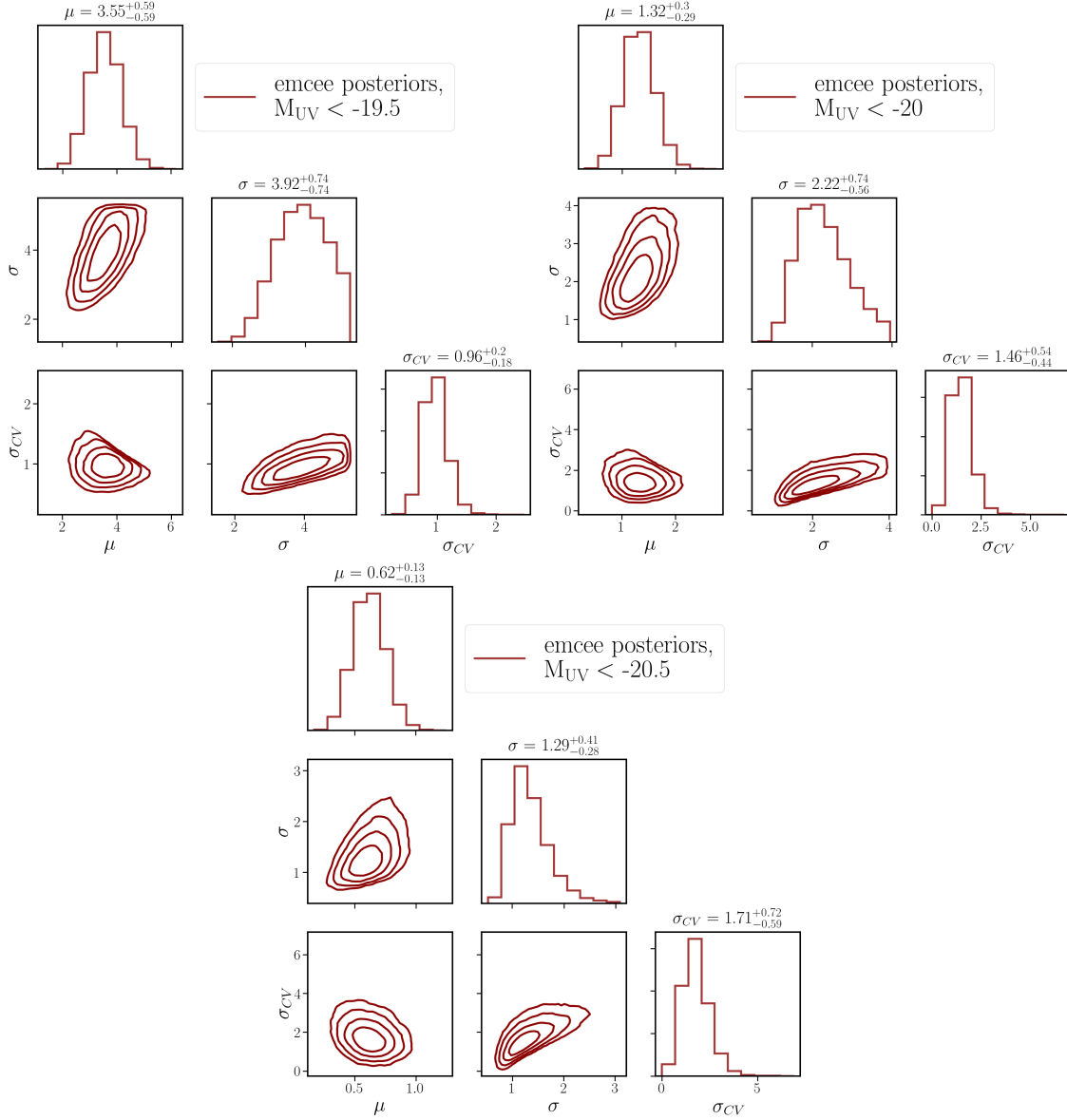


Figure 8. Posterior distributions of the MCMC-fitting described in Section 2.4.2. The fitted quantities are the mean and variance. Contours correspond to 0.5, 1, 1.5 and 2 σ confidence regions.